Scilight

Sustainable Engineering Novit

https://www.sciltp.com/journals/sen

Review

Computational Studies for Aqueous Zinc-Ion Secondary Batteries

Yu Liu [1], Yiwen Yuan [1], Rui Wang [1], Lvhao Duan [1], Rongguan Lv [1], Yingna Chang [1], Huayu Wu [1], Xiaoli Yan [1], Rong Xing [1,*] and Rudolf Holze [2,3,4,*]

[1] Institute of New Energy on Chemical Storage and Power Sources, School of Green and Low Carbon, Yancheng Teachers University, Yancheng 224000, China
[2] Institut für Chemie, AG Elektrochemie, Technische Universität Chemnitz, D-09107 Chemnitz, Germany
[3] Confucius Energy Storage Lab, School of Energy and Environment, Southeast University, Nanjing 210096, China
[4] State Key Laboratory of Materials-Oriented Chemical Engineering, School of Energy Science and Engineering, Nanjing Tech University, Nanjing 211816, China
* Correspondence: rxing@yctu.edu.cn (R.X.); rudolf.holze@chemie.tu-chemnitz.de (R.H.)

How To Cite: Liu, Y.; Yuan, Y.; Wang, R.; et al. Computational Studies for Aqueous Zinc-Ion Secondary Batteries. *Sustainable Engineering Novit* **2025**, *1*(1), 6. https://doi.org/10.53941/sen.2025.100006

Received: 15 September 2025
Revised: 22 October 2025
Accepted: 28 November 2025
Published: 9 December 2025

Abstract: Aqueous zinc-ion secondary batteries (AZIBs) have emerged as a leading candidate for next-generation energy storage due to their high safety, low cost, and environmental compatibility. Despite these advantages, challenges such as zinc dendrite formation, hydrogen evolution reaction (HER), cathode dissolution, and sluggish ion kinetics hinder their widespread commercialization. Theoretical computational studies have become indispensable in addressing these issues by providing atomic-level insights into reaction mechanisms, material properties, and interfacial behaviors. This comprehensive review systematically examines the role of computational methods, including density functional theory (DFT), molecular dynamics (MD), finite element method, machine learning (ML), and multiscale modeling, in advancing AZIBs research. We discuss their applications in cathode material design, anode stabilization, electrolyte optimization, and interfacial engineering. Additionally, we highlight the integration of computational predictions with experimental validations and outline future directions for accelerating AZIBs development.

Keywords: aqueous zinc ion battery; computational studies; density functional theory; molecular dynamic; machine learning

1. Introduction

Since the new round of energy revolution, many disruptive technological achievements have emerged, such as shale gas and shale oil mining technologies that accelerate the global energy revolution and energy technology innovation, and renewable energy power generation technologies such as wind energy and solar energy that change the direction of energy development in large economies [1–5]. However, these intermittent renewable energies are seriously influenced by time and season when using. Therefore, an effective and reliable energy storage and conversion system is urgently required [6–9]. At present, there are many kinds of energy storage and conversion systems, such as lithium/sodium/potassium ion batteries [10–12], aqueous zinc ion batteries [13–17], lead-acid battery [18,19], Ni-Fe battery [20,21] and supercapacitors [22–26]. Among them, aqueous rechargeable zinc ion batteries (ARZIBs) have become more and more popular because metallic zinc has a large theoretical capacity of 820 mAh·g^{-1}, low reduction potential of −0.762 V versus the standard hydrogen electrode (SHE), low toxicity and abundant resources [27–30]. So far, the total number of publications for the ARZIBs is greater than 3800, as retrieved from “Web of Science” using the keywords “aqueous zinc ion battery”. Moreover, the amount of the publications is gradually soaring up every year in Figure 1a. Among all the publications, most researchers focus

on studies of cathode materials, accounting for 67.4%, as presented in Figure 1b. In addition, the research ratios in the fields of zinc anodes, electrolytes and additives are 18.7%, 6.8% and 6.2%, respectively. Other fields including separator design and modification [31,32] contribute only about 0.9%.

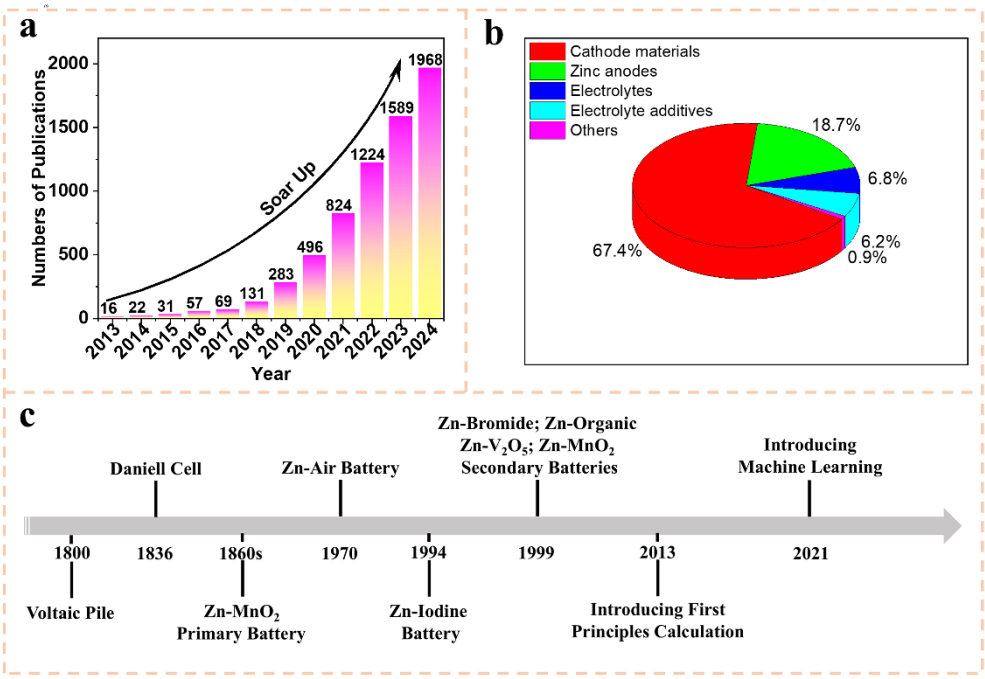

Figure 1. (**a**) Trend chart of zinc battery related published papers from 2013 to 2024. (**b**) Proportion of research on various components of zinc batteries. (**c**) Schematic diagram of the development process of zinc batteries.

In Figure 1c, the aqueous zinc battery can be traced back to the voltaic pile, which was invented by Alessandro Volta in 1799 [33]. This pile is made of stacked zinc and copper metal disks separated by cardboard soaked with brine. Based on this finding, John Frederic Daniell further developed the Zn–Cu chemistry in 1836, which is also known as the Daniell cell [34]. At that time, it was widely applied in the telegraph industry of Europe. However, it mainly appears in chemistry curricula to illustrate working principles of batteries today. The typical Daniell cell in the chemistry curricula consists of a copper plate as cathode in an aqueous copper sulfate solution and a zinc plate as anode in a zinc sulfate solution, both electrodes are connected by a salt bridge. Following the Daniell cell, the development of aqueous zinc batteries continued to evolve. In the 1860s, Zn–MnO_2 primary battery emerged as a significant advancement, offering higher energy density and stability compared to its predecessors [35]. This battery became widely used in everyday applications, such as flashlights and portable devices, due to its reliability and cost-effectiveness. By the 1970s, the Zn-Air battery gained attention for its high theoretical energy density and use of oxygen from the air as a reactant, making it suitable for applications like hearing aids and electric vehicles [36]. In 1994, the Zn-Iodine battery was introduced, showcasing potential for high energy density and environmental friendliness. However, its practical application was limited by issues such as iodine's solubility and sluggish reaction kinetics [37]. In 1999, researchers began exploring rechargeable aqueous zinc batteries, leading to the development of Zn-Bromide, Zn-Organic, Zn–V_2O_5 and Zn–MnO_2 secondary batteries [38–41]. These batteries improved upon the primary versions by allowing multiple charge-discharge cycles, though challenges like dendrite formation and limited cycle life persisted. The turn of the 21st century saw further innovations. By 2013, advancements in materials and computational science led to the integration of first-principles calculations to design next-generation zinc batteries. These approaches aim to address long-standing challenges like zinc dendrites and capacity fading, paving the way for more efficient and sustainable energy storage solutions. As recently as 2021, machine learning was firstly introduced to the field of aqueous zinc batteries, thereby significantly improving the work efficiency of researchers and promoting tremendous technological progress.

The development of high-performance aqueous zinc-ion batteries faces several fundamental challenges, including zinc dendrite formation, hydrogen evolution reaction (HER), cathode dissolution, and sluggish ion transport kinetics. While experimental techniques provide valuable macroscopic observations, they often lack the resolution needed to elucidate atomic-scale mechanisms. Computational approaches bridge this gap by offering detailed insights into electronic structures, reaction pathways, and dynamic processes at the molecular level. These methods enable the rational design of electrode materials, electrolytes, and interfaces through predictive modeling

and high-throughput screening. This review comprehensively examines five key computational techniques, including density functional theory (DFT), molecular dynamics (MD), finite element method, machine learning (ML), and multiscale modeling, and their transformative role in ARZIBs research.

In this review, we begin by providing a concise introduction to computational approaches employed in ARZIBs research. Subsequently, we showcase recent advances in the study of cathode materials, zinc anodes, and electrolytes, underscoring the critical role of theoretical simulations in elucidating material properties such as crystal structure, ion transport, defect behavior, and surface characteristics. Finally, we outline prospective research directions for computational methods aimed at enhancing the performance of rechargeable zinc batteries. It is hoped that this review will contribute to accelerating the development of computational materials science for next-generation energy storage systems.

2. Computational Methods

The rapid advancement of emerging battery technologies with high energy density demands sophisticated theoretical frameworks to complement and inspire experimental research. By integrating computational analysis with empirical measurements, researchers can systematically optimize battery performance, addressing critical challenges in energy storage. Modern computational methods applied to battery systems span multiple scales and physical principles, including quantum mechanics, molecular dynamics simulation, Monte Carlo simulation, finite element method and machine learning approaches (Figure 2).

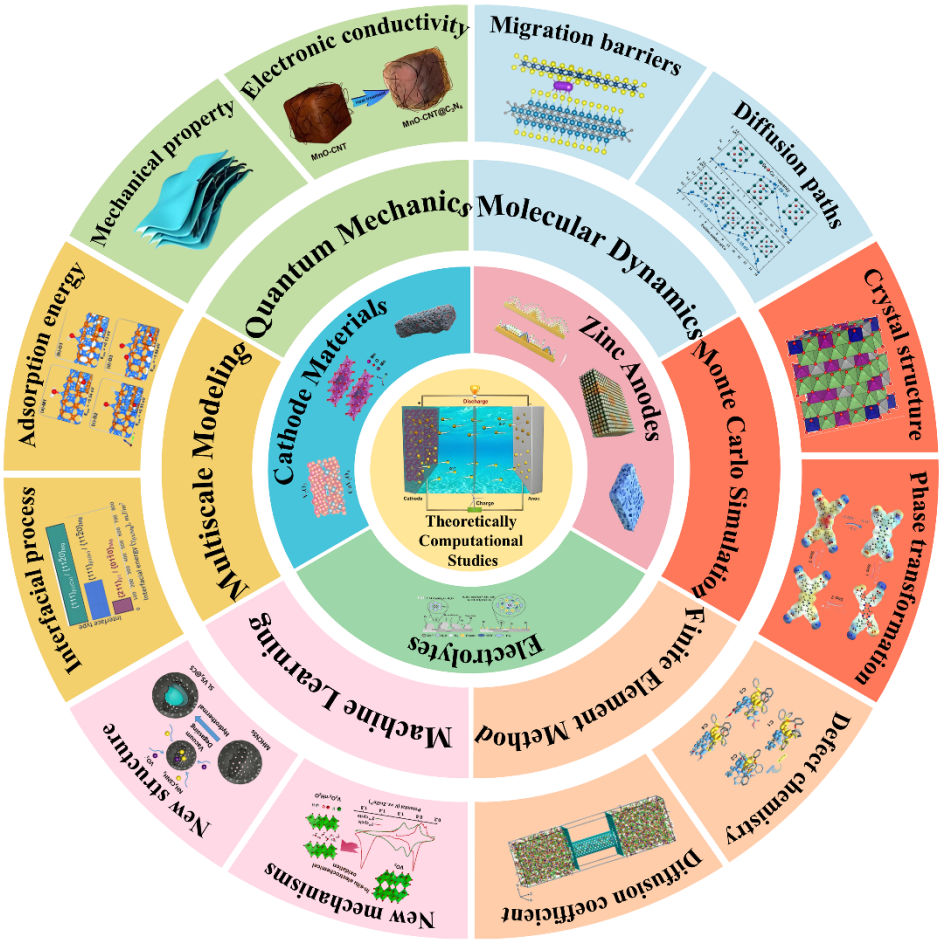

Figure 2. Schematic illustration of the main computational methods in aqueous zinc secondary batteries.

2.1. Quantum Mechanics

Quantum mechanical (QM) computational methods, particularly quantum chemistry and first-principles calculations, have become indispensable tools in modern materials science, especially in the study of rechargeable battery systems [14]. These approaches are fundamentally rooted in the principles of quantum mechanics but differ in their implementation and scope. Quantum chemistry employs quantum mechanical theory to investigate chemical systems, focusing on molecular structure, electronic properties, and reaction dynamics [42]. While it

provides valuable insights, it often incorporates empirical parameters or approximations (e.g., Hartree-Fock methods, post-Hartree-Fock corrections) to handle complex many-body interactions. This makes it particularly useful for studying molecular-scale phenomena, such as electrolyte decomposition or interfacial reactions in batteries [43]. Popular quantum chemistry software packages include Gaussian, ORCA, and Q-Chem [44], which are widely used for simulating molecular orbitals, reaction pathways, and spectroscopic properties.

In contrast, first-principles calculations, primarily based on density functional theory (DFT), operate without empirical parameters, relying solely on fundamental physical laws (e.g., the Schrödinger equation and the Hohenberg-Kohn theorems). These methods solve the electronic structure of materials through self-consistent field (SCF) iterations, enabling high-precision predictions of material properties, such as electronic structure (band gap, density of states), defect energetics (vacancy formation energies, doping effects), ion transport (diffusion pathways, migration barriers), and phase stability (thermodynamic and kinetic metastability) [45]. DFT-based calculations are implemented in software packages like VASP, CASTEP, ABINIT, Quantum ESPRESSO, and SIESTA, which are optimized for periodic boundary conditions. This is essential for modeling crystalline electrode materials. Despite their transformative impact, these methods face inherent constraints including the long computational time and extensive computational requirements [46].

In summary, quantum mechanical calculations are pivotal for decoding battery materials at atomic scales, yet their full potential requires synergistic integration with experimental validation and emerging computational paradigms.

2.2. Molecular Dynamics Simulation

Molecular dynamics (MD) is a powerful computational technique used to investigate the physical behavior of multi-particle systems by simulating the trajectories and interactions of atoms or molecules based on Newtonian mechanics [47]. By solving the equations of motion for each particle under predefined force fields, MD provides detailed atomic-scale information, including velocities, position coordinates, and accelerations. These microscopic data are then translated into macroscopic thermodynamic properties, such as heat capacity, energy, and diffusion coefficients, through the principles of statistical mechanics. Beyond revealing energy barriers and ion migration pathways, MD simulations offer critical insights into dynamic processes like phase transitions, chemical reactions, and material deformation mechanisms [48].

MD simulations are widely employed in diverse fields, including interface stability analysis (e.g., solid-electrolyte interphases in batteries), phase transition modeling (e.g., melting or crystallization), and electrolyte optimization (e.g., ionic conductivity in liquid or solid-state electrolytes). Popular MD software packages, such as LAMMPS (for large-scale systems), NAMD (optimized for biomolecules), and GROMACS (high-performance chemistry applications), cater to different research needs [44].

However, MD simulations face several inherent limitations, including (i) computational accuracy: results depend heavily on the chosen force field, which may oversimplify quantum effects or complex bonding; (ii) scale constraints: while coarse-graining techniques extend reach, MD typically simulates nanoscale systems (nm–μm) over short timescales (ns–μs); (iii) environmental sensitivity: outcomes can vary with boundary conditions, temperature/pressure controls, or initial configurations; (iv) high computational cost: atomic-level resolution demands significant resources, limiting real-time or large-system studies [49]. Despite these challenges, advances in hybrid quantum mechanics/molecular mechanics (QM/MM) methods are enhancing MD's predictive power, bridging gaps between accuracy and efficiency.

2.3. Monte Carlo Simulation

Monte Carlo (MC) method, also referred to as stochastic sampling or statistical simulation, is a computational approach that relies on repeated random sampling to obtain numerical results [50]. At its core, this technique involves constructing a probabilistic model whose parameters correspond to the solution of the target problem. By performing extensive sampling experiments and statistical observations on this model, researchers can derive the statistical characteristics of these parameters, ultimately yielding approximate solutions to complex problems.

In materials science, the MC method proves particularly valuable for investigating atomic-scale phenomena and addressing stochastic processes. For battery research, MC simulations can model a wide range of critical parameters, including but not limited to thermal behavior, safety performance, charge-discharge dynamics, cycle life, internal resistance evolution, capacity degradation, and aging mechanisms [51]. Widely used software tools for such simulations include Geant4 (for particle-matter interactions), MCNP (Monte Carlo N-Particle code for radiation transport), and FLUKA (for particle physics and radiation applications). Despite its versatility, the MC method has notable limitations. First, it typically cannot directly simulate dynamic evolutionary processes, as it primarily relies on statistical equilibrium states rather than time-dependent progression. Second, its accuracy in

force field predictions is constrained by the underlying potential models, which may not fully capture complex atomic interactions [52]. Nevertheless, the MC approach remains indispensable for problems where analytical solutions are intractable, offering a powerful alternative through probabilistic modeling and large-scale sampling.

2.4. Finite Element Method

Finite element method (FEM) is a powerful computational technique extensively employed in numerical simulations to approximate solutions for complex continuum mechanics problems. By discretizing continuous domains into a finite assembly of interconnected elements, FEM transforms intricate physical phenomena into solvable algebraic equations. This approach has become indispensable across engineering disciplines and physical sciences, particularly for scenarios where analytical solutions are intractable or non-existent [53].

In the context of rechargeable battery modeling, FEM serves as a critical tool for investigating multiphysics phenomena, including structural mechanics, thermal dynamics, and electrochemical reactions. Through the formulation of finite element equations derived from mechanical models, researchers can simulate battery behavior under various charge-discharge cycles, predicting potential failure mechanisms, vibrational characteristics, stress distribution, and deformation patterns [54]. Such simulations enable enhanced assessment of battery performance, safety, and lifespan, risk mitigation and facilitating optimized design. Widely adopted commercial FEM software, such as SolidWorks Simulation, COMSOL Multiphysics, Abaqus, and ANSYS, provide robust platforms for these analyses.

In spite of its versatility, FEM presents notable limitations. High-fidelity simulations often demand substantial computational resources, restricting their application for multi-scale or large-scale problems. Additionally, the method may encounter challenges in modeling coupled physical processes or highly nonlinear ones, such as fracture propagation or phase transitions. Pre-processing tasks (e.g., mesh generation) and post-processing (e.g., data visualization) can also be time-intensive, requiring specialized expertise [55]. Recent advancements in adaptive meshing, parallel computing, and machine learning-enhanced solvers aim to address these constraints, further expanding FEM's capabilities in battery research and beyond.

2.5. Machine Learning Approaches

Machine learning (ML) has emerged as a transformative paradigm in the development and optimization of rechargeable battery systems, offering data-driven solutions to complex electrochemical challenges. By employing sophisticated algorithms to analyze multidimensional datasets encompassing charge-discharge characteristics, impedance spectra, and degradation signatures, ML enables the extraction of non-intuitive structure-property relationships that conventional physical models often fail to capture [56]. The methodological framework typically involves supervised learning for state-of-health estimation, unsupervised techniques for anomaly detection in operational batteries, and reinforcement learning for autonomous optimization of charging protocols. These approaches leverage advanced computational architectures, including convolutional neural networks for spatial feature extraction from microscopic data and graph neural networks for modeling particle-to-particle interactions in electrode materials [57].

The deployment of ML in battery research has yielded significant advancements across multiple domains. In battery materials discovery, generative adversarial networks (GANs) have accelerated the identification of novel solid electrolyte compositions with enhanced ionic conductivity [58]. For battery management systems (BMS), recurrent neural networks enable accurate remaining-useful-life prediction by processing time-series operational data. Industrial applications demonstrate particular promise, with major automotive manufacturers implementing ML-powered digital twins to simulate battery pack performance under diverse operating conditions [59]. Open-source computational tools such as BatML and commercial platforms like COMSOL Multiphysics with ML modules are increasingly adopted to bridge the gap between fundamental research and industrial implementation.

Notwithstanding these advancements, several critical challenges persist. The scarcity of high-quality, well-annotated electrochemical datasets continues to constrain model generalizability, while the inherent trade-off between model complexity and interpretability raises concerns for safety-critical applications. Furthermore, the energy-intensive nature of deep learning model training presents sustainability concerns that somewhat paradoxically counter the environmental benefits of advanced battery systems [60]. Emerging solutions such as physics-informed neural networks and hybrid analytical-ML approaches show potential to address these limitations by incorporating domain knowledge to reduce data requirements and improve model interpretability. As the field progresses, the synergistic integration of ML with experimental characterization techniques and multiscale modeling frameworks is anticipated to play a pivotal role in realizing next-generation energy storage systems with enhanced performance, safety, and sustainability characteristics.

2.6. Multiscale Modeling

Multiscale modeling has appeared as a powerful computational framework for understanding and optimizing rechargeable batteries by bridging diverse spatial and temporal scales. At the atomic level, techniques such as DFT and MD elucidate fundamental processes, including electron transfer, ion diffusion, and interfacial reactions. These methods provide critical insights into material properties, such as electrode stability and electrolyte compatibility. At the mesoscale, phase-field models and kinetic MC simulations capture microstructural evolution, phase separation, and heterogeneous reaction kinetics, which are essential for designing high-performance electrodes and mitigating degradation mechanisms. On the macroscopic scale, continuum-based approaches, such as the pseudo-two-dimensional (P2D) model, integrate these underlying phenomena to predict battery performance under realistic operating conditions, including charge-discharge cycles and thermal effects [61].

To effectively integrate these methods, hybrid frameworks such as QM/MM and embedded multiscale models have been developed. For instance, DFT can provide accurate force field parameters for MD simulations, while MD outputs (e.g., ion transport coefficients) can inform continuum models such as FEM or P2D. Machine learning further enhances this integration by serving as a surrogate model to bridge scales, predict properties, or accelerate sampling in MC or MD simulations. Such hybrid approaches enable the prediction of battery behavior from atomic interactions to device-level performance, capturing phenomena such as dendrite growth, electrolyte decomposition, and cathode phase transitions in a unified manner.

To facilitate these simulations, a variety of computational tools are employed, ranging from atomistic software (e.g., VASP, LAMMPS) to mesoscale modeling platforms (e.g., COMSOL Multiphysics) and system-level simulation packages (e.g., PyBaMM, ANSYS Fluent). Notably, platforms like COMSOL and PyBaMM support the coupling of electrochemical, thermal, and mechanical models, enabling integrated simulations that span from electrode materials to full cell behavior. While multiscale modeling offers significant advantages, such as reducing experimental costs, accelerating materials discovery, and enabling virtual prototyping. It also presents challenges, including high computational demands, the need for accurate inter-scale coupling, and potential trade-offs in predictive accuracy due to necessary simplifications [62]. Future efforts should focus on improving data transfer protocols between scales, developing machine learning-aided coupling strategies, and validating hybrid models with operando experimental data. Nevertheless, the integration of multiscale modeling with machine learning and high-performance computing holds great promise for advancing next-generation battery technologies, offering a pathway to optimize energy density, longevity, and safety in a systematic and theoretically grounded manner.

In addition, computational methods are not merely post-hoc analytical tools but have increasingly played a predictive role in guiding experimental design. For instance, DFT-predicted band structures and diffusion barriers have directed the synthesis of doped MnO_2 and V_2O_5 cathodes with enhanced electronic conductivity and Zn^{2+} mobility, which were subsequently validated by electrochemical tests. Similarly, MD simulations of solvation structures have informed the selection of electrolyte additives that suppress dendrite formation, as confirmed by in situ microscopy. This synergy accelerates material discovery and optimization, reducing reliance on trial-and-error approaches.

3. Cathode Materials

While numerous cathodes, i.e., positive electrode, materials have been explored for ARZIBs, their practical deployment is often hindered by insufficient understanding of Zn^{2+} storage mechanisms and structural degradation during cycling. Recent advances in theoretical approaches, particularly DFT and ab initio molecular dynamics (AIMD), have provided critical insights into host-guest interactions, enabling rational design of high-performance cathodes. Furthermore, high-throughput computational screening, augmented by machine learning, has accelerated the discovery of optimized cathode materials with tailored electronic structures and reduced Zn^{2+} migration barriers [63]. These theoretical studies not only complement experimental observations but also establish predictive frameworks for identifying stable, high-capacity cathode materials, thereby bridging the gap between fundamental research and practical ARZIBs development.

3.1. Metal Oxides

Manganese- and vanadium-based oxides (e.g., MnO_2, VO_2, V_2O_5, $ZnMn_2O_4$) have served as particularly promising materials for ARZIBs due to their distinctive structural characteristics and multivalent redox chemistry. These materials exhibit multiple polymorphic structures, such as α-, β-, γ-, and δ-phases of MnO_2 and layered versus tunnel configurations of V_2O_5, which significantly influence their electrochemical behavior [64]. The structural transformations during Zn^{2+} intercalation typically involve multiple phase transitions through Zn^{2+} insertion/extraction without breaking Mn–O/V–O bonds, thereby leading to characteristic multi-step voltage

profiles. Furthermore, the specific transition metal composition (Mn, V, or mixed metals) and crystal structure determine the Zn^{2+} ordering schemes and intermediate phases formed during cycling, which directly impact the voltage profiles and rate capability [65]. These structural characteristics also govern Zn^{2+} diffusion kinetics and phase transition dynamics, critically determining the electrochemical performance. Computational studies have provided essential insights into the ionic diffusion pathways, intercalation mechanisms, and defect chemistry of these materials, complementing experimental characterization. In this section, we systematically review computational investigations of a few major kinds of oxide cathodes.

3.1.1. Manganese Dioxide

The electrochemical performance of MnO_2-based cathodes in ARZIBs has been significantly improved through strategic modifications, including doping, compositing, and interface engineering. Theoretical calculations, particularly DFT and MD simulations, have played a pivotal role in elucidating the atomic-scale mechanisms behind these enhancements. This section reviews key findings from computational studies, highlighting how these methods provide critical insights into electronic structure modifications, ion diffusion kinetics, and structural stability, ultimately guiding the design of high-performance battery materials.

DFT calculations have revealed that doping MnO_2 with transition metals or heteroatoms can profoundly alter its electronic structure, thereby enhancing electrochemical performance. For instance, vanadium-doped δ-MnO_2 (V-δ-MnO_2) exhibits a higher cohesive energy (1.591 eV) compared to pristine δ-MnO_2 (1.567 eV), attributed to strong V–O bonds (644 $kJ \cdot mol^{-1}$), which mitigate structural collapse during Al^{3+} intercalation [66]. Similarly, nitrogen and sulfur co-doping (NS-MnO_2 in Figure 3a) narrows the bandgap from 1.14 eV to 0.3 eV, improving electronic conductivity and reducing the Zn^{2+} diffusion energy barrier from 1.03 eV to 0.72 eV [67], as shown in Figure 3b. This computational prediction guided the experimental synthesis of NS-MnO_2, which demonstrated significantly improved rate capability and cycling stability, confirming the theoretical forecast. Axial nitrogen coordination via triethanolamine (TEA) disrupts the spin symmetry of MnO_2, leading to enhanced spin polarization and near-closure of the Hubbard gap. Partial density of states (PDOS) analysis confirms increased occupancy of Mn e_g orbitals, facilitating electron transfer and improving reaction kinetics [68]. Additionally, Ni doping in δ-MnO_2 upshifts the d-band center of Mn, enhancing charge delocalization and electron transfer kinetics, as demonstrated by DFT simulations [69].

Theoretical studies have provided detailed insights into ion diffusion and intercalation processes in MnO_2-based cathodes. In hydrated layered δ-MnO_2, DFT combined with EXAFS revealed a unique Zn^{2+} storage mechanism involving inner-sphere complexation. Zn^{2+} preferentially occupies triple-corner-sharing (TCS) sites, forming a protruding "Zn–Mn dumbbell" structure (Figure 3c) with a characteristic distance of ~4.2 Å, which stabilizes the host lattice during cycling. Crystal water reduces Zn^{2+} diffusion barriers to 0.32 eV, compared to 1.03 eV in dehydrated spinel MnO_2, by charge shielding and enabling hydrated ion migration [70].

For Zn-MnO_2 batteries, DFT and MD simulations demonstrate that SiO_2 colloidal particles exhibit strong adsorption energies for Mn^{3+} (~10.76 eV), promoting heterogeneous nucleation and ordered MnO_2 deposition during charging. The preferential adsorption of Mn-ions over Zn^{2+} is further validated by MD snapshots showing Mn^{3+} enrichment near SiO_2 surfaces [71]. Similarly, in Zn–Cl_2 batteries (Figure 3d), MnO_2 adsorbents stabilize Cl_2 cathodes by forming intermediate Cl_{ads}@MnO_2 species with an adsorption energy of −4.93 eV, facilitating electron transfer and reducing charge transfer resistance [72]. Structural stability is a critical factor in the long-term performance of MnO_2-based cathodes. DFT studies on Al-intercalated α-MnO_2 (AMO) identified the most stable Al-intercalation site (formation energy: −4.17 eV), where Al^{3+} doping elongates Mn–O bonds (2.05 Å vs. 1.92 Å in pristine MnO_2) and reduces the bandgap, facilitating charge transfer and Zn^{2+} diffusion [73]. In N-doped carbon/MnO_2 composites, pyrrolic N-atoms induce electron delocalization at the MnO_2 interface, elongating Mn–O bonds (2.23 Å vs. 1.93 Å) and lowering the Mn valence state, which weakens electrostatic repulsion during Zn^{2+}/H^+ insertion [74].

Interface engineering also plays a crucial role. MD simulations reveal that shorter interface distances between MnO_2 and carbon substrates in Figure 3e, facilitated by CTAB nanomicelles, enhance Zn^{2+} diffusion coefficients, optimizing rate performance [75]. Additionally, hydroxylated manganese oxide (H-MnO_2) in Figure 3f exhibits weakened H^+ adsorption energy (−0.23 eV vs. −0.77 eV in MnO_2) and enhanced Zn^{2+} adsorption (−2.05 eV vs. −1.17 eV), suppressing Mn dissolution and promoting Zn^{2+} insertion [76].

DFT calculations have also elucidated the mechanisms behind the enhanced bifunctional catalytic activity of MnO_2-based materials in zinc-air batteries. For example, anchoring Co_3O_4 nanoparticles onto the MnO_2(110) surface activates neighboring Mn sites (Mn1 and Mn2), with Bader charge analysis showing substantial electron transfer (~0.86 e) from Co_3O_4 to MnO_2. This electron transfer shifts the Mn 3d states to lower energies, reducing

the density of states at the Fermi level and weakening hydrogen bonding with OH/OOH intermediates, thereby lowering thermodynamic barriers for oxygen reduction and evolution reactions (ORR/OER) [77]. Substitution of Mn^{4+} with V^{4+} or Cr^{4+} in hollandite α-MnO_2 further enhances catalytic performance. Cr-substitution, in particular, promotes preferential reduction to stable Cr^{3+}, limiting the formation of Jahn-Teller active Mn^{3+} ions and maintaining structural stability during discharge. Cr-substituted MnO_2 also exhibits higher initial discharge voltages (2.50 V vs. 2.11 V for pristine) and lower volume expansion (3.1% vs. 5.2%) [78].

Theoretical calculations and simulations have provided a foundational understanding of the mechanisms governing the enhanced performance of MnO_2-based cathodes in aqueous batteries. By elucidating electronic structure modifications, ion diffusion pathways, and structural stability, these studies have guided the design of high-performance materials. Future research should focus on integrating multi-scale simulations with experimental validation to further optimize battery performance and explore new material systems.

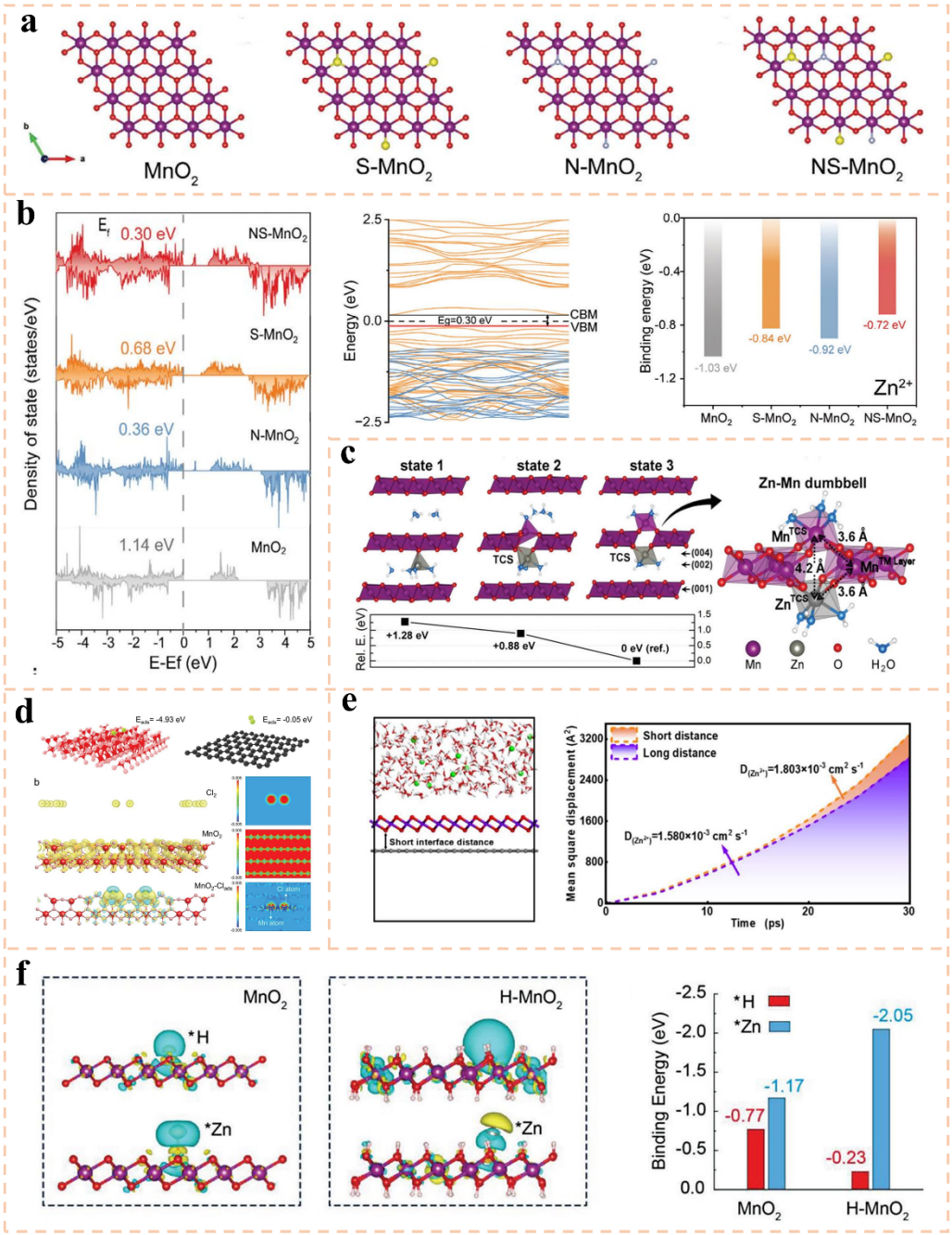

Figure 3. (**a**) Structure diagrams of MnO_2 and dual anions doped MnO_2; (**b**) Total density of states of the MnO_2 based materials, band structure diagram of the NS-MnO_2 and binding energies of Zn^{2+} with the MnO_2 based materials. Reproduced with permission from ref. [67]. Copyright 2025, Wiley. (**c**) Zn-intercalated structures and relative energies. Reproduced with permission from ref. [70]. Copyright 2019, The Royal Society of Chemistry (RSC). (**d**) DFT calculations of the role of MnO_2 in an aqueous Zn–Cl_2@MnO_2 battery. Reproduced with

permission from ref. [72]. Copyright 2023, Wiley. (**e**) Initial MD simulation models for Zn^{2+} diffusion in short interface distance sample and overall Zn^{2+} diffusion coefficient. Reproduced with permission from ref. [75]. Copyright 2024, RSC. (**f**) Charge density difference and adsorption energy of Zn/H on MnO_2 and H-MnO_2. Reproduced with permission from ref. [76]. Copyright 2024, Wiley.

3.1.2. Vanadium Oxides

Theoretical calculations have also been instrumental in elucidating the mechanisms behind the enhanced performance of vanadium-based cathodes in ARZIBs. For instance, DFT simulations demonstrated that Al-doping in V_2O_5 reduces the Zn^{2+} diffusion barrier from 0.36 eV to 0.09 eV, significantly improving reaction kinetics. This prediction was experimentally validated, with Al-doped V_2O_5 achieving a high capacity of 480 $mAh \cdot g^{-1}$ and excellent rate performance. Moreover, Al doping transforms the electronic structure of V_2O_5 from a semiconductor (bandgap of 2.26 eV) to a metallic conductor by introducing defect states near the Fermi level, thereby enhancing electrical conductivity [79]. Similarly, cation nanoconfinement in ultrathin V_2O_5 nanosheets was shown to weaken Zn^{2+} interactions with dangling oxygen atoms, further lowering diffusion barriers [80]. MD simulations of deep eutectic solvent (DES) electrolytes, such as 90 m $ZnCl_2$ + 45 m choline chloride, revealed the formation of polynuclear aggregates (e.g., $[ZnCl_6]^{4-}$) and superhalides (e.g., $[ZnCl_4]^{2-}$), which stabilize anion insertion in layered vanadium oxides [81]. These findings highlight the critical role of electrolyte composition in enabling reversible anionic redox reactions, contributing to higher energy densities.

Further DFT studies have explored the effects of doping and intercalation on the electrochemical properties of V_2O_5. Nitrogen interstitial doping was found to reduce the Zn^{2+} diffusion barrier from 1.46 eV to 0.75 eV, altering the diffusion pathway from vertical interlayer to planar intralayer diffusion (Figure 4a), thereby improving rate capability [82]. Similarly, Cr^{3+} pre-intercalation in hydrated vanadium oxide (VOH) narrowed the bandgap and reduced Zn^{2+} adsorption energy, leading to a high capacity of 405 $mAh \cdot g^{-1}$ and exceptional cycling stability [83]. Polyaniline (PANI) intercalation into V_2O_5 expanded the interlayer spacing and weakened Zn^{2+}-host lattice interactions, achieving a capacity of 480 $mAh \cdot g^{-1}$ [84]. Additionally, oxygen-defect-rich $V_2O_{5-x} \cdot nH_2O$ exhibited a lower Zn^{2+} diffusion barrier (0.26 eV vs. 0.39 eV in pristine VOH) in Figure 4b and improved electronic conductivity, resulting in a volumetric capacity of 711.9 $mAh \cdot cm^{-3}$ [85]. These studies underscore the importance of tailoring electronic structures and interlayer environments to optimize cathode performance. The presence of structural water in $V_2O_5 \cdot nH_2O$ has been shown to enhance electrochemical performance by acting as additional host sites for electron transfer, leading to stronger Zn^{2+} ionization and higher open-circuit voltage, as displayed in Figure 4c. DFT-D2 calculations revealed that structural water reduces Zn^{2+} diffusion barriers (0.66 eV for hydrated V_2O_5 vs. 1.40 eV for dry V_2O_5) and stabilizes the material through negative formation energies [86]. Defect engineering, such as oxygen vacancies, enables 3D Zn^{2+} diffusion along the c-axis in Figure 4d, unlike the restricted ab-plane diffusion in pristine V_2O_5, improving kinetics and capacitive storage [87]. Furthermore, pre-intercalation of Na^+ in V_2O_5/carbon composites or NH_4^+ in NH_4^+-V_2O_5 reduces charge transfer barriers and enhances Zn^{2+} migration [88,89]. These strategies highlight the dual role of structural modifications in facilitating ion diffusion and stabilizing the cathode structure.

Deng et al. demonstrated that electrocatalytic oxygen evolution reactions (OER) coupled with interface oxidation in VO_2 induce a phase transformation into $V_5O_{12} \cdot 6H_2O$, enabling a nearly two-electron reaction and super-theoretical capacity [90]. Wang et al. revealed that Co-substitution in VO_2 ($Co_{0.03}V_{0.97}O_{2-x}$ in Figure 4e) stabilizes the structure and enhances conductivity, with Zn^{2+} diffusion barriers reduced to 0.261 eV compared to pristine VO_2 (0.636 eV) [91]. DFT calculations have provided critical insights into the impact of defect engineering and heterostructures on the electrochemical performance of VO_2-based cathodes. Li et al. showed that oxygen vacancies (V_0) in VO_2 widen ion diffusion tunnels and lower Zn^{2+} diffusion barriers (0.24–0.71 eV vs. 0.78 eV for pristine VO_2), significantly improving ionic conductivity [92]. Wang et al. further demonstrated that oxygen vacancies in VO_2 (O_d-VO_2) modulate Zn^{2+} adsorption energy (−0.039 eV), enabling reversible reactions, while graphene heterointerfaces in Figure 4f enhance electron transport, synergistically boosting performance [93]. These studies highlight the importance of DFT in guiding defect engineering and heterostructure design for optimized cathode materials. Luo et al. investigated the heterostructured VO_2-carbon cloth (H-VO_2@CC) composite, revealing a built-in electric field at the interface that enhances electron/ion transport kinetics and provides additional active sites for Zn^{2+} storage [94]. Zhang et al. introduced the descriptor Δd-p to evaluate the energy difference between dopant d-band centers and oxygen p-band centers, demonstrating that Mo-doped VO_2(B) with the smallest Δd-p (3.26 eV) exhibits optimized electronic structure and superior electrochemical performance [95]. These findings emphasize the role of DFT in unraveling complex interfacial interactions and electronic effects.

The synergistic effects of dopants and composite materials have been extensively explored using DFT. Guan et al. revealed that H-doping in VO_2 shifts the valence electron conduction band, facilitating electron transfer and increasing oxygen defects, which aligns with experimental observations [96]. Liu et al. demonstrated that the VO_2(B)/Ta_4C_3 MXene heterojunction exhibits metallic characteristics due to charge transfer, significantly enhancing conductivity and reducing Zn^{2+} diffusion barriers to 0.34 eV [97]. These studies illustrate how DFT-guided material design can lead to high-performance cathodes for ARZIBs.

In addition, DFT analyses reveal that oxygen vacancies in Na-doped hydrated $NH_4V_4O_{10}$ (NaNVOH) significantly narrow the band gap, improving electronic conductivity and facilitating Zn^{2+} diffusion. Zhang et al. demonstrated that optimal interlayer H_2O/NH_4^+ content and oxygen vacancies in NaNVOH reinforce bond strength and reduce electrostatic interactions, leading to higher Zn^{2+} diffusion coefficients (10^{-12}–10^{-11} $cm^2 \cdot s^{-1}$) and structural stability [98]. Similarly, Cui et al. showed that oxygen vacancies in $NH_4V_4O_{10-x}$@rGO lower the Zn^{2+} migration energy barrier (1.67 eV for intercalation and 1.08 eV for deintercalation) compared to pristine $NH_4V_4O_{10}$ (1.97 eV and 2.04 eV, respectively), enhancing ion kinetics [99]. Charge density difference analyses further confirm that oxygen vacancies redistribute electrons around vanadium atoms, weakening Zn^{2+}-host interactions and stabilizing the structure during cycling. These findings highlight the synergistic effects of defect engineering and interlayer regulation in optimizing cathode materials, as evidenced by improved capacity (519 $mAh \cdot g^{-1}$) and cycling stability (90% retention over 3000 cycles) [98].

DFT calculations have also shed light on the importance of hydrogen bond networks and atomic-level design in enhancing the performance of ARZIBs electrode materials. Li et al. revealed that hydrogen bonds (N–H•••O and O–H•••O in Figure 4g) in layered vanadium and manganese oxides stabilize the structure and lower the proton diffusion barrier, facilitating rapid transport via the Grotthuss mechanism [100]. In another study, Liu et al. demonstrated that unsaturated Ni/V centers and short metal-metal distances in $Ni_{0.22}V_2O_5$ (Figure 4h) enhance electron transfer from O to Ni, improving conductivity and reducing the Zn^{2+} migration barrier to 0.64 eV. These insights were validated using climbing-image nudged elastic band (cNEB) methods, which identified favorable Zn^{2+} diffusion pathways along the ab-plane [101]. Such theoretical studies underscore the critical role of atomic-level design in optimizing electrode materials for high-performance ARZIBs.

Defect engineering and heterointerface formation have been identified as key strategies for improving Zn^{2+} diffusion kinetics in ARZIBs. Wang et al. reported that a self-generated heterointerface between $Zn_3(OH)_2V_2O_7(H_2O)_2$ (ZOV) and NaV_2O_5 reduces the Zn^{2+} diffusion energy barrier from 1.726 eV to 1.002 eV, accelerating ion transport [102]. Similarly, sulfur doping in $H_2V_3O_8$ introduces oxygen defects, reducing the bandgap from 1.24 eV to 0.69 eV and lowering the Zn^{2+} adsorption free energy from −2.16 eV to −2.65 eV, thereby enhancing electronic conductivity and storage capacity [103]. These findings highlight the transformative potential of defect engineering and heterointerface design in cathode materials.

The influence of crystal orientation and dopants on Zn^{2+} diffusion has been extensively investigated through DFT simulations. Cao et al. found that Zn^{2+} diffusion along the (001) plane in $Zn_3V_2O_7(OH)_2 \cdot 2H_2O$ (ZnVO) nanowires faces a lower energy barrier (0.31 eV) compared to non-basal diffusion in ZnVO flakes (0.89 eV) in Figure 4i, explaining the superior performance of nanowire structures [104]. Additionally, Liu et al. showed that Al^{3+} doping in $Zn_3(OH)_2V_2O_7 \cdot 2H_2O$ reduces the Zn^{2+} diffusion barrier from 1.93 eV to 0.34 eV, significantly enhancing rate capability and cycling stability [105]. These studies emphasize the importance of crystallographic and dopant engineering in optimizing cathode materials for ARZIBs.

3.1.3. Other Metal Oxides

As for other metal oxides, Bai et al. demonstrated through DFT calculations that oxygen vacancies in $Cu_3V_2O_7(OH)_2 \cdot 2H_2O$ (CVO-SS-2) significantly reduce the adsorption energy of Zn^{2+} ions, thereby enhancing the reversibility of Zn^{2+} adsorption/desorption processes and improving the material's conductivity and interfacial activity [106]. Similarly, Li et al. employed DFT to show that Zn doping in Co_3O_4 induces an insulator-to-metal transition, which drastically enhances electrical conductivity and charge transfer kinetics, leading to superior rate capability and cycling stability [107]. DFT calculations have also been widely used to explore the effects of defect engineering and doping on spinel cathode materials as mentioned above. Long et al. revealed that Ni doping in $Ni_xMn_{3-x}O_4$@C reduces the band gap and transforms the material from a semiconductor to a metallic state, facilitating electron transport and Zn^{2+} diffusion [108]. Mallick et al. further demonstrated that defect engineering in $Zn_{0.65}Ni_{0.58}Mn_{1.75}O_4$ introduces cation vacancies and oxygen defects, resulting in metallic behavior and enhanced Zn^{2+} storage performance [109]. Additionally, Shao et al. showed that K and Fe double doping in $ZnMn_2O_4$ induces oxygen defects and electronic rearrangement, lowering the formation energy and improving

structural stability [110]. These studies collectively underscore the importance of DFT in guiding the rational design of spinel cathode materials through defect engineering and doping.

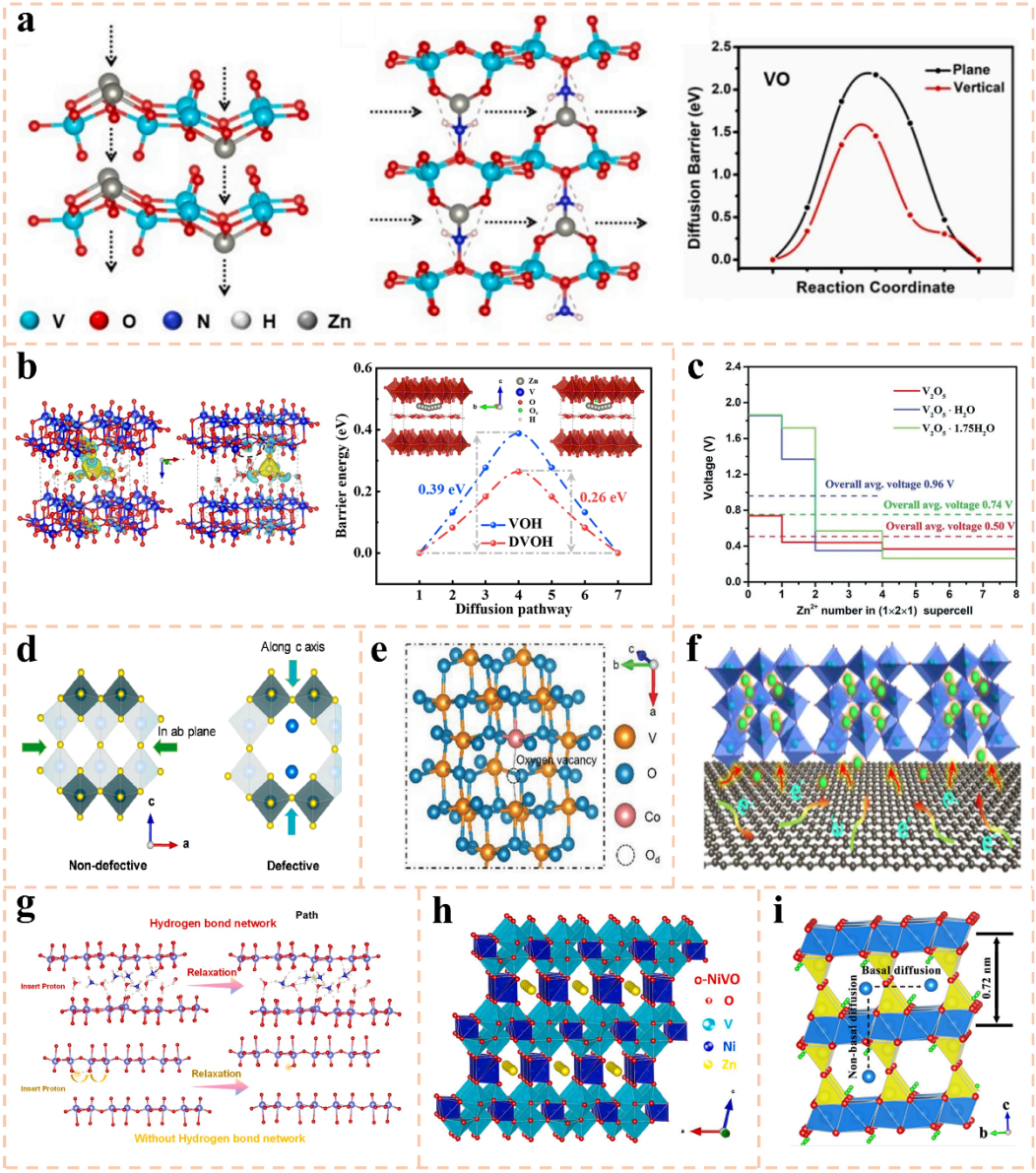

Figure 4. (**a**) Schematic illustration of Zn^{2+} diffusion pathway in VO, NVO and energy barrier of Zn^{2+} diffusion in VO. Reproduced with permission from ref. [82]. Copyright 2023, Elsevier. (**b**) Charge density difference and diffusion barrier profiles of Zn^{2+} transport in VOH and DVOH. Reproduced with permission from ref. [85]. Copyright 2022, RSC. (**c**) Average voltages for vanadium oxides at different states of Zn^{2+} insertion. Reproduced with permission from ref. [86]. Copyright 2019, RSC. (**d**) Schematic illustration of V_2O_5 and O_d-V_2O_5. Reproduced with permission from ref. [87]. Copyright 2021, Elsevier. (**e**) Crystal structure diagram of O_d-CoVO. Reproduced with permission from ref. [91]. Copyright 2024, Wiley. (**f**) Schematic illustration for the electron and ion transfer at the interface. Reproduced with permission from ref. [93]. Copyright 2020, Elsevier. (**g**) Schematic comparison of proton transport under hydrogen bond network and without hydrogen bond network. Reproduced with permission from ref. [100]. Copyright 2022, Elsevier. (**h**) Zn^{2+} migration sites along the b-axis in o-NiVO. Reproduced with permission from ref. [101]. Copyright 2022, Elsevier. (**i**) The possible diffusion pathways of Zn^{2+} ion in the crystal structures. Reproduced with permission from ref. [104]. Copyright 2021, Elsevier.

The role of interfacial effects and charge storage mechanisms in ARZIBs cathode materials has been extensively investigated using DFT. Tan et al. demonstrated that the intercalation of polyaniline (PANI) into MoO_3 (PMO) significantly reduces the Zn^{2+} diffusion barrier compared to Na^+-intercalated MoO_3 (NMO), enhancing Zn^{2+} mobility and cycling stability [111]. Teng et al. revealed that oxygen vacancies in mesoporous Co_3O_{4-x} narrow the bandgap, improving electronic conductivity and OH^- adsorption energy [112]. Furthermore, Wang et

al. combined DFT with crystal orbital Hamilton population (COHP) analysis to show that Ti-substitution in $Na_{0.44}MnO_2$ weakens Mn-O bonds and increases charge density near the Fermi level, thereby improving Mn redox kinetics [113]. These insights highlight the pivotal role of computational methods in optimizing material design and understanding charge storage mechanisms. Recent studies have leveraged DFT and ab initio molecular dynamics (AIMD) simulations to advance the design of electrode materials for energy storage systems. Wei et al. demonstrated that oxygen vacancies in $NiCo_2O_4$ nanosheets reduce the band gap and widen the Co 3d orbital, enhancing conductivity and charge transfer [114]. Zhang et al. employed AIMD simulations to investigate the ion-exchange mechanism in inverse-spinel Mg_2VO_4, showing that the exchange of Mg^{2+} and Zn^{2+} reduces the diffusion energy barrier of Zn^{2+} [115]. These theoretical insights provide a foundation for designing high-performance electrode materials, as validated by experimental results.

3.2. Metal Nitrides

In the case of metal nitrides, Bai et al. used DFT to show that nitrogen vacancies in VN clusters (N_v-VN/C-SS-2) reduce the Zn^{2+} adsorption energy from −0.18 eV to −0.08 eV in Figure 5a, promoting reversible Zn^{2+} adsorption/desorption and increasing the number of active sites [116]. Similarly, Bian et al. demonstrated via DFT that NH_4^+ ions formed during the in situ transformation of VN quantum dots (VNQD) in Figure 5b lower the diffusion barrier for Zn^{2+} in vanadium oxides, thereby improving ion transport [117]. Chen et al. further illustrated that Al doping in VN (Al-VN) modulates the electronic structure and expands lattice spacing, as supported by DFT analysis of Al–N and Al–O bonding, leading to reduced charge transfer resistance [118]. DFT calculations have also been instrumental in elucidating interfacial and catalytic behaviors in VN-based electrodes. In a study of Zn^{2+}-mediated catalysis for fast-charging ARZIBs, DFT revealed that the Zn^{2+}–VN system exhibits near-optimal adsorption energy for *OH intermediates (~1.23 eV), facilitating rapid water dissociation kinetics [119]. Luo et al. employed DFT to analyze Zn^{2+} adsorption on carbon-coated VN nanorods (VNC), showing that the carbon layer weakens Zn^{2+}–cathode interaction and prolongs the Zn–N bond length (from 2.0233 Å in VN to 2.2246 Å in VNC, as displayed in Figure 5c), thereby enhancing reaction kinetics [120]. Furthermore, in the context of Zn–air batteries, Posadzy et al. combined experimental synthesis with DFT-based electronic structure analysis to evaluate transition metal nitride/carbon nanofiber composites. Their calculations underscored the synergistic effect of Co and Fe in CoFe–Fe_3N/CNF, which optimizes the adsorption energy of oxygen intermediates and improves both oxygen evolution and reduction reactions. Density of states (DOS) analysis indicated a reduced bandgap, consistent with enhanced electrical conductivity and electrocatalytic performance [121]. Theoretical investigations further extend to complex hybrid structures and reaction energetics. For example, DFT was applied to analyze the VN/TiO_2/TiN (VNTONC) hybrid, revealing that the incorporation of TiO_2 and TiN reduces Zn^{2+} adsorption energy on VN surfaces and lowers diffusion energy barriers at interfacial regions, promoting faster ion transport. DOS results indicated higher electronic density near the Fermi level at the TiN–VN interface, improving charge transfer. Charge density difference plots further confirmed electron accumulation at interfaces, stabilizing the structure during cycling. These insights align with experimental observations of improved pseudocapacitive behavior and higher Zn^{2+} diffusion coefficients in VNTONC (10^{-9}–10^{-10} $cm^2 \cdot s^{-1}$) [122,123]. In another study, Chen et al. used DFT to validate the spontaneity of the discharge process in oxygen-doped VN (O-VN), with a Gibbs free energy of −5.693 kcal/mol, and emphasized the reversible conversion between vanadium valence states, contributing to a high capacity of 705 $mAh \cdot g^{-1}$ [124]. Jung et al. utilized DFT to compare adsorption energies of bromine species on tungsten oxynitride (WON), revealing that WN (111) surfaces exhibit stronger adsorption (e.g., −11.01 eV for Br_3^-) than WO_3 or graphene, highlighting WON's superior ability to capture polybromides and enhance reaction kinetics in zinc–bromine flow batteries [125].

3.3. Metal Phosphides

As for metal phosphides, DFT calculations on $Na_4Fe_3(PO_4)_2P_2O_7$ (NFPP) uncovered a synergistic Na^+/Zn^{2+} co-intercalation mechanism, which enhances structural stability and ion diffusion kinetics compared to single-ion intercalation. The co-intercalation process was shown to yield lower energy barriers for Zn^{2+} diffusion (Figure 5d), particularly in the presence of Na^+, thereby facilitating improved reaction kinetics [126]. In another study, phenylamine (PA)-intercalated $VOPO_4 \cdot 2H_2O$ was examined using the climbing-image nudged elastic band (CI-NEB) method. The results demonstrated that expanding the interlayer spacing from 7.4 Å to 16.5 Å markedly reduced the Zn^{2+} diffusion barrier from 0.13 eV to 2.3×10^{-4} eV, resulting in an ultrahigh diffusion coefficient of approximately 5.7×10^{-8} $cm^2 \cdot s^{-1}$. This theoretical finding corroborated experimental observations that capacity is strongly influenced by interlayer spacing [127]. Collectively, these studies underscore the vital role of computational approaches in guiding the design of high-performance cathode materials through the optimization

of ion transport and thermodynamic properties. In addition, DFT calculations indicated that introducing oxygen vacancies in bilayer-$VOPO_4 \cdot 2H_2O$ nanosheets significantly narrows the bandgap from 1.5 eV to 0.2 eV, thereby improving electronic conductivity and enabling Zn^{2+} diffusion with an ultralow energy barrier of 0.08 eV [128]. Similarly, DFT analyses of crystalline NiCoP@amorphous $NiCoPO_4$ (C-NiCoP@A-$NiCoPO_4$) revealed that the amorphous phosphate shell promotes charge redistribution at the heterointerface, which enhances OH^- adsorption and electron transfer. This was supported by a calculated adsorption energy of −2.39 eV for OH^- [129]. First-principles simulations further confirmed that shorter bond lengths in the amorphous phase (e.g., Co–O in PO_4, 1.85 Å) compared to the crystalline phosphide (Co–P, 2.427 Å) contribute to improved structural stability and faster reaction kinetics [129]. Mott-Schottky analysis validated a 57-fold increase in carrier concentration in oxygen-deficient bilayer-$VOPO_4 \cdot 2H_2O$, consistent with DFT predictions [128]. DFT calculations have also been applied to study the Zn^{2+} storage mechanism and structural stability of $Zn_3V_4(PO_4)_6$ (ZVP) as a cathode material. Simulations were carried out using the Vienna Ab initio Simulation Package (VASP) with the projector-augmented-wave (PAW) method, a cutoff energy of 520 eV, and the PBE-GGA functional. A Hubbard U correction (U_{eff} = 4.0 eV) was applied to accurately describe the strong electron correlations in V 3d states. Structural models of $Zn_{3-x}V_4(PO_4)_6$ ($0 \le x \le 2$) were fully relaxed to determine ground-state configurations, and equilibrium voltages were derived from internal energy differences. The results indicated that Zn^{2+} extraction preferentially occurs at Zn2 sites in Figure 5e, with formation energies of 3.307 eV (Zn2) versus 5.1603 eV (Zn1) for the first ion removal, and 3.4323 eV (Zn2) versus 5.2208 eV (Zn1) for the second. The computed average voltages of 1.65 V ($0 \le x \le 1$) and 1.69 V ($1 \le x \le 2$) agreed well with experimental values (~1.6 V). Furthermore, DFT-predicted lattice parameters and volume changes (2.4%) were consistent with the low-strain behavior observed via in situ XRD, clarifying the exceptional cycling stability of ZVP [130]. These outcomes highlight the value of DFT in designing stable cathode materials for rocking-chair zinc-ion batteries.

3.4. Metal Sulfides

In studies of metal sulfides, Chen et al. employed DFT to demonstrate a marked reduction in the Zn^{2+} diffusion barrier from 0.6635 eV in pristine V_3S_4 to 0.6041 eV in a VN/V_3S_4 heterostructure, which is attributable to favorable interfacial effects that promote ion mobility and rate performance [131]. In a related study, Li et al. combined DFT with experimental analysis to show that introducing cobalt doping and sulfur vacancies into Ni_3S_2 significantly enhances the OH^- adsorption energy (from 0.925 eV to −2.425 eV), thereby improving surface reactivity and electronic conductivity near the Fermi level [132]. Although not all studies include computational validation, as seen in the work by Tian et al., which relied on XRD, XPS, and HRTEM, the synergy between theory and experiment remains essential for elucidating reaction pathways and material behavior [133]. Li et al. used DFT to confirm the stability and expanded interlayer spacing (0.96 nm) in nitrogen-doped carbon-intercalated MoS_2 nanocages (C–MoS_2–NC), which resulted in a reduced Zn^{2+} diffusion barrier of 0.342 eV compared to 0.869 eV in bulk MoS_2 [134]. Similarly, Liu et al. revealed via DFT that cobalt doping promotes the transition from semiconducting 2H-MoS_2 to metallic 1T-MoS_2, substantially enhancing electrical conductivity and reducing the diffusion barrier to 0.20 eV in the presence of crystal water [135]. Further extending this concept, Li et al. demonstrated that intercalation of conductive PEDOT polymer not only widens the interlayer gap to 1.29 nm but also introduces a proton co-intercalation mechanism that screens coulombic interactions and facilitates rapid Zn^{2+} transport [136]. Studies indicate that the metastable 1T phase of MoS_2 in Figure 5f exhibits a lower Zn^{2+} diffusion barrier than its 2H counterpart, owing to its metallic conductivity and octahedral coordination geometry [137,138]. The incorporation of monolayer water further expands interlayer spacing and screens electrostatic interactions, leading to an exceptionally low diffusion barrier of 0.047 eV and enhanced Zn^{2+} adsorption. Electronic structure analysis via density of states (DOS) confirms increased electron density near the Fermi level in 1T-MoS_2, primarily contributed by Mo 4d orbitals, which improves electrochemical activity and open-circuit voltage [137]. In VS_2, the formation of vanadium vacancies was shown to be energetically favorable, effectively transforming the local stoichiometry toward VS_4 and opening alternative Zn^{2+} migration pathways along the c-axis [139]. This defect-rich structure strengthens Zn^{2+} binding, as evidenced by more negative intercalation energies (−3.56 eV with 50% V-vacancies vs. −2.45 eV in pristine VS_2), while Bader charge analysis indicates reduced charge transfer, suggesting weakened host–guest interaction and improved ion kinetics. Similar theoretical approaches have been applied to other material systems. Ren et al. identified the metallic character of V_5S_8 and a low Zn^{2+} diffusion barrier of 1.47 eV, superior to that of VS_4 (1.98 eV), rationalizing its high rate capability [140]. Tan et al. reported an ultra-low barrier of 0.29 eV for Zn^{2+} diffusion in 1T-VS_2, supported by DOS and electron localization function analyses confirming metallic behavior [141]. Wang et al. further highlighted the role of interfacial engineering, showing strong binding (−0.49 eV) between defective MoS_x and carbon nanosheets and a reduced diffusion barrier

of ~0.2 eV, underscoring the benefit of hybrid structures in facilitating ion transport [142]. Beyond conventional intercalation cathodes, DFT has illuminated catalytic and adsorption mechanisms in conversion-type and alkaline systems. Xu et al. revealed that MoS_2 promotes electron transfer in Te@MoS_2 composites, strengthening Zn^{2+} adsorption (−1.83 eV vs. −1.55 eV in pure Te) and reducing energy barriers for ZnTe formation and decomposition, confirming the catalytic role of MoS_2 in tellurium redox reactions [143]. In an alkaline electrolyte environment, Yu et al. used DFT to show strong OH^- adsorption on $NiCo_2S_4$ surfaces (2.25 eV), which was further enhanced in a carbon hybrid structure (2.43 eV), underscoring the importance of interfacial design in improving reaction kinetics [144].

3.5. Metal Selenides

In the work of Bai et al., DFT calculations demonstrated that selenium vacancies in $VS_{0.5}Se_{2-x}$-SS significantly reduce the adsorption energy of Zn^{2+} ions from −0.866 eV to −1.224 eV. This reduction promotes more reversible adsorption/desorption processes and introduces additional active sites for zinc ion storage. The lowered energy barrier facilitates faster ion diffusion and improved reaction kinetics, thereby contributing to the material's high specific capacity and superior rate performance [145]. Similarly, Chen et al. employed DFT to illustrate that selenium vacancies in $MoSe_2$ ($MoSe_2$–V_{Se}) decrease the diffusion barrier for Zn^{2+} ions from 0.396 eV to 0.201 eV. These negatively charged vacancies not only reduce spatial hindrance to Zn^{2+} migration but also enhance electronic conductivity. Furthermore, DFT-derived binding energy differences (ΔE) under illuminated and dark conditions offered insights into the photo-enhanced spontaneity of reactions and energy release during zinc ion insertion and extraction [146], as presented in Figure 5g. Complementing these studies, Aghdam et al. conducted DFT simulations to probe Zn^{2+} and H^+ migration and adsorption behaviors. Using the climbing-image nudged elastic band (CI-NEB) method, they identified a diffusion energy barrier of 0.84 eV for Zn^{2+} in c-$ZnMnO_3$, which is higher than that for H^+ (0.48 eV), suggesting kinetically favored proton diffusion. Additionally, the considerably lower adsorption energies for Zn^{2+} (0.11–0.13 eV) compared to H^+ (1.01–1.81 eV) indicate a preferential insertion of Zn^{2+} ions, consistent with the observed two-stage insertion process and pronounced pseudocapacitive behavior of the electrochemically oxidized MnSe cathode [147]. In another relevant study, Wu et al. applied DFT to investigate the zinc-ion storage mechanism in ultrathin VSe_2 nanosheets. The calculations affirmed the metallic character of VSe_2, indicated by a high density of states near the Fermi level, which supports efficient electron transfer during redox reactions. CI-NEB analysis further revealed an energy barrier of 0.91 eV for Zn^{2+} diffusion between stable adsorption sites competitive with other layered cathodes, helping to explain the high experimental diffusion coefficient (~10^{-8} $cm^2 \cdot s^{-1}$) and excellent cycling stability [148].

3.6. Prussian Blue Analogues

In the field of Prussian blue analogs (PBAs), Cui et al. demonstrated via DFT that phase transitions significantly influence the diffusion energy barriers for Cl^-, K^+, and Zn^{2+} in KFeMnHCF and KZnHCF structures. Notably, Zn^{2+} exhibited the highest barrier in post-transition KZnHCF due to repulsive interactions with Zn sites. Density of states (DOS) analysis further indicated a reduced band gap in KZnHCF (0.99 eV) compared to KFeMnHCF (1.15 eV), suggesting enhanced electronic conductivity after phase transition, which is consistent with experimental electrochemical impedance spectroscopy (EIS) results [149]. Similarly, Fu et al. applied DFT and CI-NEB to model Zn^{2+} diffusion in Mn@Fe_1-PBA, identifying an optimal adsorption site at the hollow position surrounded by C≡N bridges and a low diffusion barrier of 0.58 eV, as shown in Figure 6a. This value is comparable to Na^+ migration in $Na_xFeFe(CN)_6$ and substantially lower than that in KZnHCF (~3.5 eV), corroborating the excellent rate capability observed experimentally [150]. In several studies, DFT calculations have been instrumental in clarifying the interactions between electrode materials and active species, thereby elucidating the origins of enhanced electrochemical performance. Li et al. used DFT to compute adsorption energies of iodine species (I^-, I_2, I_3^-, ICl) on vanadium-based Prussian blue analogues (V-PBA) in Figure 6b, revealing a strong preference for vanadium sites. Charge redistribution led to an upshift in the vanadium d-band center and increased metallic character of adsorbed iodine, facilitating faster reaction kinetics and suppressing the shuttle effect in Zn–I batteries [151]. Puthiyaveetil et al. also employed DFT to demonstrate stable adsorption of polypyrrole (PPy) on V-PBA with an adsorption energy of −1.89 eV, confirming charge transfer from PPy to V-PBA. This interaction enhances electronic conductivity and promotes Zn^{2+} adsorption, contributing to improved capacity and cycling stability in aqueous zinc metal batteries [152]. DFT-based simulations have further been applied to examine interfacial phenomena and ion transport in PBA electrodes. Qian et al. used DFT to calculate I_2 adsorption energies on different PBA surfaces, finding that transformed ZnFe-PBA exhibited the most negative adsorption energy, indicating superior iodine confinement and cycling stability [153]. Wang et al. utilized DFT to

analyze density of states (DOS) and Zn^{2+} migration pathways in $Ag_3Fe(CN)_6$, identifying low-energy diffusion paths and confirming the metallic character of the material, which underpins its high electronic conductivity and rate performance [154]. Such computational analyses provide critical understanding of redox behavior, ion diffusion, and interfacial processes, guiding the rational design of high-performance PBA electrodes. Additional DFT investigations have focused on reaction energetics and functional group effects. Gao et al. computed Gibbs free energy changes (ΔG) for iodide oxidation on Prussian blue (PB) and iodine-preembedded Prussian blue (PBI) in Figure 6c, revealing a lower energy barrier on PBI (1.27 eV) compared to PB (2.63 eV), which was attributed to Fe–I bond formation. This result aligns with experimental observations of reduced polarization and improved kinetics in zinc–iodine batteries [155]. In a specific application to functionalized materials, DFT was used to probe the role of hydroxyl groups in enhancing the electrochemical behavior of manganese hexacyanoferrate (MnHCF) cathodes. Adsorption energies of –OH groups at various atomic sites (N, C, K, Fe, Mn) were evaluated, with the Mn site showing the most favorable energy (−4.14 eV), indicating preferential hydroxyl binding. This result was consistent with XPS and FTIR data confirming hydroxyl enrichment after hydrogen annealing. Furthermore, DFT revealed that hydroxyl groups reduce the Zn^{2+} adsorption energy to approximately −0.35 eV, promoting stronger Zn^{2+} capture and activating both Fe^{3+}/Fe^{2+} and Mn^{3+}/Mn^{2+} redox couples [156]. These findings provide a mechanistic basis for the improved multi-redox reactivity and specific capacity observed in OH-rich MnHCF cathodes, highlighting how theoretical approaches uncover structure-property relationships in functionalized battery materials.

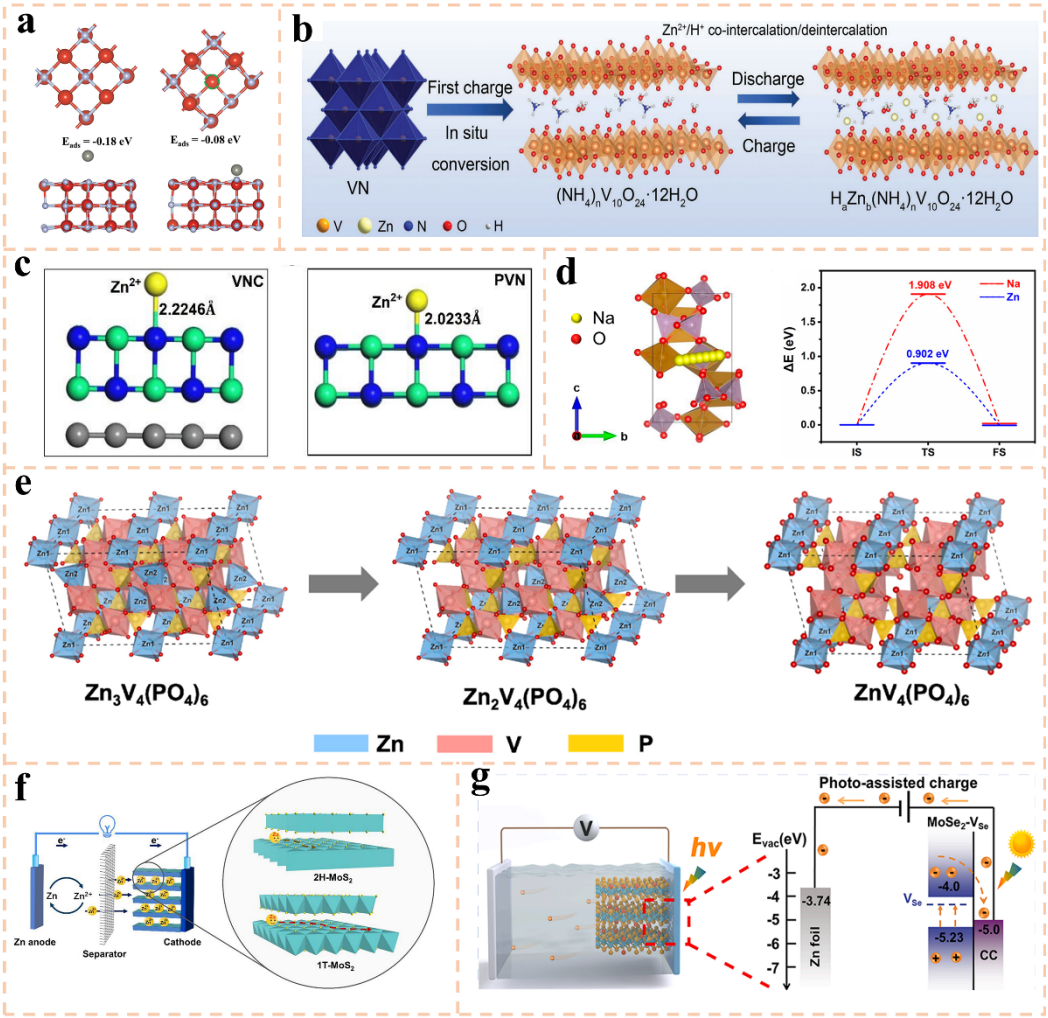

Figure 5. (**a**) Model of VN without/with vacancies and the adsorption/desorption of Zn^{2+} on the N_V-VN/C-SS-3 and N_V-VN/C-SS-2. Reproduced with permission from ref. [116]. Copyright 2024, Wiley. (**b**) Schematic illustration of the significant electrochemical transformation during the discharge/charge process. Reproduced with permission from ref. [117]. Copyright 2024, Wiley. (**c**) Zinc ion adsorption structures on VNC and PVN. Reproduced with permission from ref. [120]. Copyright 2024, RSC. (**d**) Diffusion pathway and diffusion energy barriers of Na^+ and Zn^{2+} in $Na_2Fe_3(PO_4)_2P_2O_7$. Reproduced with permission from ref. [126]. Copyright 2023, ACS. (**e**) Schematic illustration of the reversible phase transformation between $Zn_3V_4(PO_4)_6$ and $ZnV_4(PO_4)_6$. Reproduced with

permission from ref. [130]. Copyright 2022, Elsevier. (**f**) Illustration of the rechargeable Zn//MoS_2 battery system. Reproduced with permission from ref. [138]. Copyright 2020, Elsevier. (**g**) The photo-responsive zinc ion battery schematic diagram with $MoSe_2$-V_{Se} cathode. Reproduced with permission from ref. [146]. Copyright 2024, Elsevier.

3.7. Organic Materials

Theoretical and computational methodologies are integral to advancing our understanding of organic cathode materials for ARZIBs. Among these, DFT stands out as a powerful tool for optimizing molecular geometries, elucidating electronic structures, and evaluating intermolecular interactions. For example, Ding et al. demonstrated through DFT simulations that molecules rich in hydroxyl groups, such as DHT, facilitate the formation of planar and symmetric two-dimensional hydrogen-bonded networks, as presented in Figure 6d. This structural feature not only enhances stability but also promotes efficient proton transport via the Grotthuss mechanism [157]. Complementing these findings, molecular dynamics (MD) simulations conducted by Hong and colleagues revealed how sulfate ions promote the formation of water clusters in biphasic electrolytes, effectively suppressing the dissolution of organic species [158]. Furthermore, DFT analyses performed by Hua et al. on dihydro-octaazapentacene (DOP) unveiled its aromatic character, electrostatic potential profile, and redox-active sites, confirming a bipolar charge storage mechanism involving both Zn^{2+}/H^+ and ClO_4^- [159]. Together, these computational insights, validated experimentally, provide a foundational understanding of structure–property correlations and reaction mechanisms, paving the way for rational material design. Additionally, DFT calculations illustrated that an asymmetric charge distribution in m-DMBQ reduces the bandgap and lowers the LUMO energy, resulting in improved electronic conductivity and elevated discharge voltages [160], as displayed in Figure 6e. In another study on DHTAP derivatives, DFT simulations indicated that electron-withdrawing substituents such as –F and $–NO_2$ effectively tune frontier orbital energies, narrow the bandgap, and enhance redox kinetics, which are supported by ultraviolet photoelectron spectroscopy and UV-Vis reflectance measurements [161]. DFT calculations also have been extensively employed to decode the electrochemical behavior, structural evolution, and electronic characteristics of organic cathodes. Zhang et al. used DFT to demonstrate that the p-type organic material DHTAT possesses a narrow bandgap of 3.652 eV, which enhances electronic conductivity, and identified –NH– groups as favorable sites for ClO_4^- adsorption, with a binding Gibbs free energy of −11.283 kcal·mol^{-1} [162]. Kundu et al. applied DFT to model Zn^{2+} insertion into p-Chloranil, predicting a minimal volume change of −2.7% and a rotated molecular column configuration in Figure 6f that accommodates Zn^{2+} ions more effectively [163]. In a study on perylene diimide derivatives (2PDI), Li et al. confirmed through DFT that H^+ and Zn^{2+} co-insertion leads to the formation of a stable $(2PDI)_2(H^+)_6(Zn^{2+})$ complex, with a strong Zn^{2+} binding energy of −6.34 eV [164]. Molecular electrostatic potential (MESP) analyses and frontier orbital calculations further aided in identifying electrophilic sites and rationalizing redox potentials and charge transfer behavior.

The critical role of DFT calculations in examining ion storage behavior, electronic properties, and redox mechanisms in organic electrode materials is further highlighted across several studies. Wang et al. computed the cohesive energy of BBPD and NTCDA crystals, finding that BBPD exhibits stronger intermolecular interactions (−2.58 eV) than NTCDA (−1.71 eV), which correlates with its superior structural stability and reduced solubility. Electrostatic potential mapping identified C=N groups as preferred redox centers over C=O groups, supporting a H_3O^+ insertion mechanism, while Gibbs free energy calculations confirmed the thermodynamic preference for proton over Zn^{2+} coordination [17]. In another study, Wang et al. used DFT to analyze the molecular electrostatic potential and frontier orbitals of TTPQ, demonstrating that Zn^{2+} and H^+ co-insertion reduces the bandgap and improves electronic conductivity, thereby accelerating reaction kinetics [165]. Wang and collaborators employed DFT to determine the energy levels of tetrathiafulvalene (TTF) in various oxidation states in Figure 6g and the absorption energies of $ZnCl_4^{2-}$ anions, validating a multi-step redox reaction and anion insertion mechanism [166].

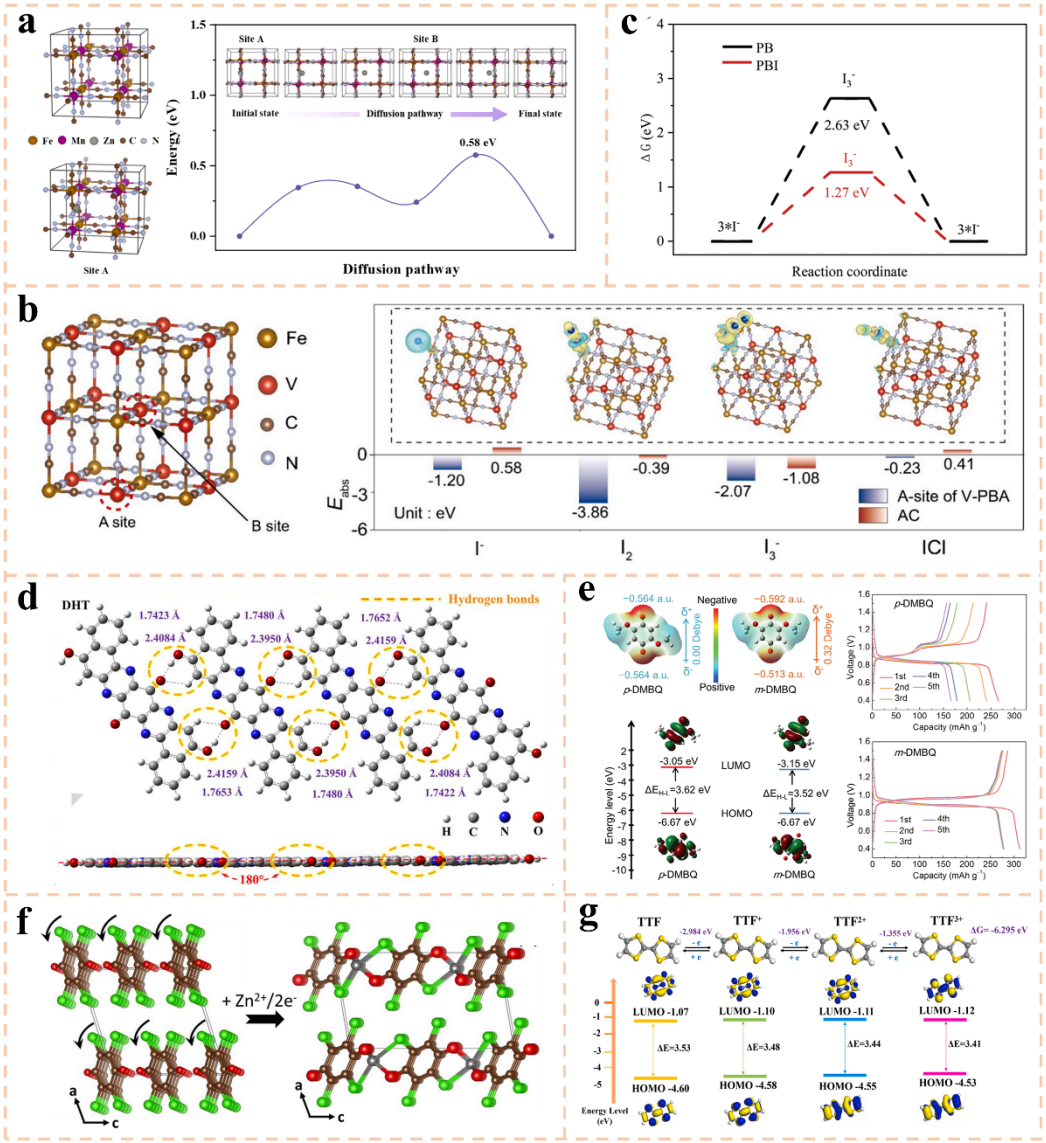

Figure 6. (**a**) Mechanistic study of Zn ion diffusion barrier and pathway in Mn@Fe1-PBA. Reproduced with permission from ref. [150]. Copyright 2025, Elsevier. (**b**) Structural model and calculated adsorption energy of iodine species (I^-, I_2, I_3^- and ICl) on A site of V-PBA. Reproduced with permission from ref. [151]. Copyright 2025, Elsevier. (**c**) Gibbs free-energy diagrams of I^- oxidation reaction in PB and PBI. Reproduced with permission from ref. [155]. Copyright 2023, Wiley. (**d**) Front view and side view of the optimized structure of intermolecular hydrogen bonds in DHT. Reproduced with permission from ref. [157]. Copyright 2025, Wiley. (**e**) Calculated MEP distributions, frontier molecular orbital energy levels and voltage profiles of p-DMBQ and m-DMBQ. Reproduced with permission from ref. [160]. Copyright 2024, Wiley. (**f**) The curved arrows in structural model show the direction of the rotation of p-Chloranil molecular columns upon Zn^{2+} insertion. Reproduced with permission from ref. [163]. Copyright 2018, ACS. (**g**) Calculated ΔG values for transformation and calculated HOMO/LUMO spatial distributions, energies, energy gaps (Δ*E*) of TTF, TTF^+, TTF^{2+}, TTF^{3+}. Reproduced with permission from ref. [166]. Copyright 2023, Elsevier.

3.8. Others

In terms of organic-inorganic hybrid cathodes, Ding et al. utilized DFT to screen amino acid-based coatings, identifying isoleucine as an effective modifier for α-MnO_2 due to its stable adsorption energy (−1.45 eV) mediated by Mn–N bonds. Subsequent MD simulations illustrated that isoleucine enriches Zn^{2+} concentration near the electrode while limiting water penetration, thereby mitigating manganese dissolution and improving cycling stability [167]. In the work of Sang et al., DFT calculations indicated that intercalating PEDOT into V_2O_5 not only expands the interlayer spacing but also modifies the electronic structure by shifting the Fermi level toward the conduction band, thereby improving electronic conductivity. This alteration results in a reduced energy barrier for Zn^{2+} migration (1.26 eV) in PEDOT-V_2O_5 compared to 1.46 eV in pristine V_2O_5, promoting faster ion diffusion

and electron transfer [168]. Likewise, Luo and colleagues applied DFT to demonstrate that the MOF-5-V composite possesses an ultra-low Zn^{2+} diffusion barrier of 0.32 eV, substantially lower than those of pure VO_2 (0.61 eV) and $Zn_2V_2O_7$ (0.50 eV), which correlates with excellent rate performance and cycling durability [169]. Additional density of states (DOS) analysis near the Fermi level revealed strong orbital hybridization within MOF-5-V, suggesting enhanced charge transfer and structural integrity. Further DFT studies continue to reveal structure–property relationships in hybrid cathodes. Ma et al. showed that the EDA-VO hybrid exhibits metallic conductivity arising from p–d hybridization near the Fermi level, along with an ultralow diffusion barrier of 0.78 eV for Zn^{2+} along a preferred pathway, accounting for its exceptional rate capability [170]. Nagaraj et al. employed hybrid DFT (B3LYP-D3) to optimize the crystal structures of VEG and Zn-VEG, confirming that zinc preintercalation lowers the formation energy for subsequent Zn-ion insertion and improves structural stability [171]. Using DFT at the B3LYP/6-31G level, Sariyer et al. computed binding energies associated with Zn^{2+} and H^+ coordination in a polyphosphazene-based cathode, demonstrating the thermodynamic favorability of multi-cation insertion, which aligns with experimental observations of mixed ion storage [172]. Together, these computational efforts deepen the understanding of ion storage mechanisms, electronic properties, and kinetic processes, thereby supporting the rational design of high-performance cathodes for ARZIBs. Some key computational parameters were further summarized in Table 1.

Table 1. Summary of key computational parameters for cathode materials.

Material Category	Modification Strategy	Bandgap/eV (before/after)	Diffusion Barrier/eV (before/after)	Ref.
δ-MnO_2	NS-MnO_2	1.14/0.3	-/-	[67]
MnO_2	N-coordinated MnO_2	2.29/1.72	-/-	[68]
MnO_2	Al-intercalated MnO_2	0.85/-	-/-	[73]
MnO_2	Hydroxylated MnO_2	-/-	0.56/0.18	[76]
V_2O_5	Al-doped V_2O_5	2.26/-	0.36/0.09	[79]
V_2O_5	NH_4 nanoconfinement	-/-	1.02/0.64	[80]
V_2O_5	Nitogen doped V_2O_5	1.6/1.1	2.19/0.75	[82]
V_2O_5	Defect-rich $V_2O_{5-x}nH_2O$	-/-	0.39/0.26	[85]
V_2O_5	Structural H_2O	-/-	1.40/0.66	[86]
VO_2	Oxygen vacancy	-/-	0.78/0.24	[92]
$NH_4V_4O_{10}$	Oxygen deficiency	-/-	1.97/1.67	[99]
$Ni_{0.22}V_2O_5$	Unsaturated Ni/V centers	-/-	-/0.64	[101]
$H_2V_3O_8$	Oxygen deficiency	1.24/0.69	-/-	[103]
$Zn_3V_2O_7(OH)_2{\cdot}2H_2O$	Orientation effect	-/-	0.89/0.31	[104]
V_2O_3	Al-doped V_2O_3	-/-	1.93/0.34	[105]
VN	Carbon-enveloped VN	2.1/1.63	-/-	[120]
$VOPO_4{\cdot}2H_2O$	Oxygen vacancy	1.5/1.3	0.13/0.08	[128]
MoS_2	N-doped carbon motifs	0.82/0.64	0.869/0.342	[134]
$MoS_2{\cdot}nH_2O$	Cobalt doping	1.46/0.4	0.92/0.2	[135]
MoS_2	H^+ modified MoS_2	-/-	0.97/0.41	[136]
V_5S_8	Tunnel structure	1.0/-	1.98/1.47	[140]
$MoSe_2$	Se deficiency	-/-	0.369/0.201	[146]
VSe_2	Ultrathin	-/-	-/0.91	[148]
Mn-PBA [a]	Iron hexacyanoferrate	-/-	3.5/0.58	[150]
DHTAP [b]	Electron-withdrawing groups (–F and $–NO_2$)	2.79/2.11	-/-	[161]
DHTAT [c]	/	-/3.652	-/-	[162]
$VO_2{\cdot}Zn_2V_2O_7$	MOFs derivative	-/-	-/0.32	[169]
EDA-VO [d]	Organic-inorganic hybrid	-/-	-/0.78	[170]

[a] prussian blue analogues; [b] 5,12-dihydro-5,7,12,14-tetraazapentacen; [c] 5,12-dihydro-5,6,11,12-tetraazatetracene; [d] ethylenediamine–vanadium oxide.

4. Zinc Anodes

As discussed above, DFT is also widely utilized to examine adsorption energetics and interfacial characteristics of zinc anodes. For example, research by Cao et al. employed DFT to demonstrate that $ZnWO_4$ exhibits a stronger adsorption energy for Zn^{2+} ions, ranging from −0.47 to −0.52 eV, compared to bare zinc (−0.38 eV), which contributes to more uniform nucleation and effective dendrite suppression. Complementary COMSOL Multiphysics simulations illustrated how such modified interfaces alter the electric field distribution, thereby

encouraging homogeneous ion flux and minimizing localized deposition [173]. These computational insights directly guided the experimental fabrication of $ZnWO_4$-modified anodes, which indeed showed uniform Zn deposition and suppressed dendrite formation, as visualized by in situ microscopy. In a similar manner, Gao et al. applied DFT to analyze the adsorption of electrolyte species such as $EMIM^+$ and $TFSI^-$ on zinc surfaces, confirming the development of a water-deficient Helmholtz layer that reduces parasitic reactions. Phase-field simulations in Figure 7a further provided visual evidence of uniform ion transport and inhibited dendrite formation on engineered surfaces [174]. The integration of multi-scale computational methods offers profound insights into the interfacial processes governing zinc deposition. Huang et al., through DFT calculations, identified that an in situ formed $CuZn_5$ alloy layer possesses a relatively low zinc binding energy (−1.83 eV), which enhances deposition kinetics and improves cycling stability [175]. Additional studies, such as those by Ling et al. and Peng et al., utilized DFT to explore ion diffusion barriers and selective ion adsorption, respectively. Ling's group found that a $ZnSnF_6/Sn/ZnF_2$ interface considerably lowers the diffusion energy barrier for Zn^{2+} ions, facilitating rapid transport [176]. Meanwhile, Peng's team showed that bentonite clay promotes zinc ion permeation while repelling sulfate anions, thereby reducing side reactions [177]. Electric field and ion concentration simulations via COMSOL, as applied in studies by Shu et al. in Figure 7b, further emphasize how protective layers such as CeO_2 foster uniform deposition through electric field homogenization [178].

Molecular dynamics and finite element simulations provide further mechanistic clarity at various scales. For instance, Zhao et al. used MD simulations to reveal how specific electrolyte additives, such as tris(2-cyanoethyl) borate, restructure the solvation shell of zinc ions, thereby lowering water activity and facilitating desolvation [179]. Concurrently, FES illustrated the role of angstrom-scale channels in two-dimensional metal–organic frameworks in homogenizing ion flux and suppressing dendritic growth [180], as presented in Figure 7c. Other researchers, including Hu et al. and Lee et al., applied DFT to probe surface reconstruction and defect-mediated deposition behavior. Hu's work illustrated preferential zinc deposition on the (101) crystal plane in the presence of dimethyl sulfoxide, while Lee's simulations highlighted the strong orbital hybridization between zinc adatoms and carbon defect sites, effectively immobilizing nuclei and inhibiting aggregation [181,182].

Moreover, several studies employed DFT to compare zinc affinity across different materials and crystal planes. Luo et al. reported that the $AgZn_3$ alloy offers a Zn binding energy of −0.84 eV, markedly higher than that of pure Zn or Ag, suggesting improved nucleation kinetics [183]. Pan et al. found that the ZnOHF (110) surface has a Zn^{2+} adsorption energy of −1.84 eV, greatly exceeding that of the Zn (001) surface, which promotes uniform plating [184]. Qin et al. also used DFT to confirm that nitrogen-doped carbon (3D-NC) supplies highly favorable adsorption sites within its porous architecture, improving zinc deposition uniformity [185]. Electric field and ion transport simulations performed in COMSOL consistently underscore the importance of interface design in achieving uniform current distribution. Studies by Liu et al. and Song et al. demonstrated that modified layers such as g-C_3N_4 and boron nitride nanofiber (BNNF) effectively mitigate the "tip effect" by evenly distributing the electric field and concentrating Zn^{2+} ions, thereby discouraging dendritic growth [186,187].

These computational approaches not only offer atomic- and meso-scale understanding of interfacial phenomena but also bridge theoretical predictions with experimental validations. Collectively, they establish a robust foundation for the rational design of highly reversible and durable zinc anodes, paving the way for next-generation energy storage systems.

5. Electrolytes

5.1. Hydrogel Electrolytes

For hydrogel electrolytes, in research conducted by Chen et al., DFT calculations were instrumental in determining binding energies between polymer chains and solvent molecules. These results indicate that dimethyl sulfoxide (DMSO) exhibits a preferential interaction with polyacrylonitrile (PAN) and poly(vinyl alcohol) (PVA), whereas water shows a stronger affinity for polyacrylamide (PAM), ultimately leading to nanoscale phase separation [188]. Complementing these findings, MD simulations captured conformational changes in polymer chains across different solvents, confirming the emergence of a homogeneous network in DMSO and aggregation in water, which is a key factor underpinning the structural integrity and ionic conductivity of the hydrogel. Further insights were provided by Guo et al., who employed MD simulations along with radial distribution function (RDF) analysis to examine the solvation structure of Zn^{2+}. Their work illustrated that 1,2-propylene glycol (1,2-PG) occupies the outer solvation shell without penetrating the inner coordination sphere, thereby diminishing water activity and improving interfacial stability [189]. Additional DFT calculations reaffirmed that 1,2-PG possesses a stronger adsorption energy on the Zn (002) surface compared to water, encouraging the development of a stable solid electrolyte interphase (SEI). In a separate investigation led by Li et al., combined DFT and MD simulations

were deployed to explore interactions between Zn^{2+} ions and trifluoroborate-terminated polyacrylamide (PAME). The outcomes highlighted that highly electronegative $–BF_3^-$ groups effectively displace water molecules within the solvation shell, curtail free water content, and enable rapid Zn^{2+} migration via electrostatic effects [190]. Binding energy analyses in Figure 7d further substantiated that Zn^{2+} ions are more readily captured by PAME segments than by water or unmodified PAM, resulting in uniform zinc deposition and effective dendrite suppression.

Additional studies employed multi-physics simulations to investigate ion transport and deposition patterns. Luo et al. used numerical modeling to simulate Zn^{2+} concentration and electric field distributions at the anode interface in Figure 7e. Their results demonstrated that embedding carboxylated multi-walled carbon nanotubes (MWCNTs) within a polyacrylamide hydrogel promotes a uniform ionic and electronic field, which in turn suppresses dendritic growth and enhances deposition homogeneity [191]. In another study, Shen et al. applied electrochemical impedance spectroscopy and Arrhenius-based modeling to determine activation energies for ion transport, revealing that highly entangled PAM networks significantly lower the energy barrier for Zn^{2+} migration, a crucial feature for high-rate battery operation [192].

Moreover, the integration of COMSOL Multiphysics simulations enabled the visualization of stress distribution and ion diffusion under mechanical deformation, offering valuable guidance for designing hydrogels with robust mechanical properties and high ionic conductivity under extreme conditions [193]. These computational strategies are further enriched by DFT analyses that probe specific molecular interactions, such as hydrogen bonding and Zn^{2+} solvation structures, paving the way for hydrogel electrolytes capable of stable operation across a wide temperature range. Wang et al. employed MD simulations to investigate changes in Zn^{2+} solvation environments within a poly(ethylene glycol)-based hydrogel under reduced water conditions. Their simulations captured a transition from water-dominated to ether-oxygen-dominated coordination, which contributes to lower water activity and sustained ionic conductivity even at elevated temperatures (90 °C) [194]. DFT-derived binding energies and electrostatic potential mapping identified favorable Zn^{2+} binding sites on polymer chains, informing the design of efficient ion-conducting pathways. In a study by Xiang et al., DFT was used to compare the electronic structures of sodium alginate (SA) and polyacrylamide (PAM). The calculations revealed that SA possesses a higher HOMO energy level (−0.82 eV) relative to both H_2O (−10.23 eV) and PAM (−7.99 eV), indicating a superior electron-donating capacity and stronger coordination with Zn^{2+} ions. The binding energy between Zn^{2+} and SA was calculated to be −27.48 eV, substantially more negative than that with PAM or water, underscoring the role of SA in promoting Zn^{2+} desolvation and uniform deposition [195]. Notably, the desolvation energy in the PAM/SA hybrid system was as low as 1.36 eV, markedly lower than in traditional electrolytes, accounting for the improved reaction kinetics. Xia et al. used MD simulations to demonstrate that a covalently cross-linked PVA/PAN hydrogel resists structural deformation under an electric field, leading to smoother and more compact zinc deposition compared to non-crosslinked analogs [196]. Similarly, Xiong et al. applied DFT to evaluate interaction energies in polycarboxylate-modified PVA hydrogels, finding that strengthened hydrogen bonding reduces free water content and suppresses parasitic reactions such as hydrogen evolution [197]. The more negative adsorption energy on the Zn (002) surface further indicated improved interfacial stability and dendrite suppression. Xu et al. integrated DFT to analyze coordination environments within an α-helical protein (α-HP) incorporated into a PVA matrix. Their results showed that Zn^{2+} ions preferentially bind to N and O atoms in the α-HP structure, resulting in a lower migration energy barrier and an ultra-high ionic conductivity of 93.8 $mS \cdot cm^{-1}$ [198]. The preferential adsorption of α-HP on the Zn (002) plane also guided dendrite-free deposition. Further supporting these findings, Abbasi et al. used DFT to compute binding energies in phosphonated graphene oxide (PGO)-modified polyacrylamide hydrogels. The introduction of PGO was shown to enhance water affinity and electrolyte retention, thereby improving ionic conductivity and reducing the activation energy for ion transport [199].

Collectively, these theoretical and computational investigations provide a molecular-level understanding of the structure-property relationships in hydrogel electrolytes. By elucidating key interactions, such as hydrogen bonding, ion coordination, polymer-solvent affinity, and interfacial adsorption, these studies form a solid foundation for the design of next-generation hydrogel electrolytes with enhanced ionic conductivity, mechanical resilience, and electrochemical stability for advanced zinc-based batteries.

5.2. Electrolyte Additives

The integration of theoretical and computational methodologies has been instrumental in advancing the design and optimization of electrolyte additives for ARZIBs. Across multiple studies, techniques such as DFT, MD, machine learning (ML), and finite element modeling (FEM) have provided deep mechanistic insights into solvation structures, interfacial phenomena, and deposition behavior. For example, Chen et al. used MD

simulations to demonstrate how a polyoxotungstate additive promotes a shift from two-dimensional to three-dimensional zinc diffusion, leading to more uniform deposition and reduced dendrite formation. The simulation results predicted improved deposition uniformity, which was confirmed by scanning electron microscopy and cycling tests, demonstrating a direct theory-to-experiment translation [200]. Similarly, Dong et al. employed a fully connected neural network to efficiently screen thousands of interface configurations, identifying a cerium-iron MOF that optimizes ion desolvation and transport, thereby suppressing hydrogen evolution and enhancing cycleability [201]. These computational strategies are frequently complemented by experimental validation, forming a powerful multimodal framework for electrolyte development. Feng's team introduced a differentiable molecular dynamics approach that refines classical force fields using empirical data, enabling high-throughput prediction of key properties such as ionic conductivity and low-temperature performance [202]. Such synergistic combinations of simulation and experiment allow for rational design of additives that modify the Zn^{2+} solvation shell, reduce water activity, and improve interfacial stability. For instance, Huang et al. used DFT to reveal stronger binding between Zn^{2+} and divalent fumarate ions compared to monovalent species, which contributes to stable solvation and suppressed hydrogen evolution [203].

Machine learning techniques further accelerate the discovery and optimization of novel electrolyte components. Luo et al. employed random forest and gradient boosting models trained on DFT-calculated molecular descriptors to predict Gutmann donor numbers in Figure 7f and identify effective high-DN additives such as isopropyl alcohol [204]. In another study, Shang et al. combined DFT, MD, and random forest modeling to correlate adsorption energy with cycling lifetime, rationalizing the superior performance of low-concentrated diols like 1,2-butanediol [205]. These data-driven approaches highlight the growing role of artificial intelligence in navigating complex chemical spaces and informing material selection.

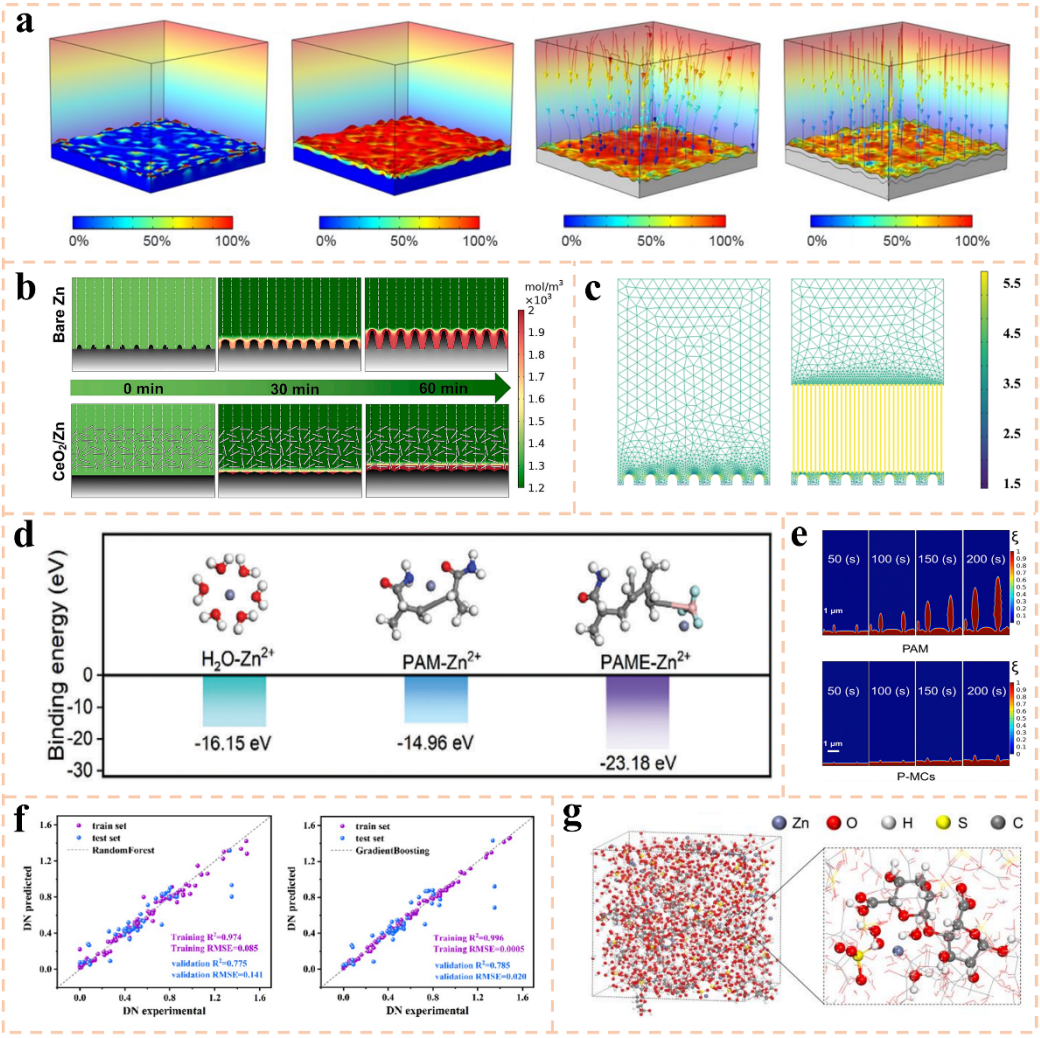

Figure 7. (**a**) Simulations of electric field and Zn ion concentration field distributions for the surface of bare Zn and Zn@IL@PPS. Reproduced with permission from ref. [174]. Copyright 2024, RSC. (**b**) COMSOL simulation of Zn^{2+} concentration distribution of bare Zn and CeO_2/Zn anodes. Reproduced with permission from ref. [178].

Copyright 2025, Elsevier. (**c**) Zn^{2+} flux distribution of bare Zn and 2D Mn-MOF@Zn anodes. Reproduced with permission from ref. [180]. Copyright 2023, Wiley. (**d**) Optimized models for DFT calculations of binding energies of Zn^{2+} in the different electrolytes. Reproduced with permission from ref. [190]. Copyright 2024, Wiley. (**e**) Electrode morphology field after Zn deposition at different times for PAM and P-MCs. Reproduced with permission from ref. [191]. Copyright 2024, RSC. (**f**) Performance of the RF and GBDT model. Reproduced with permission from ref. [204]. Copyright 2025, ACS. (**g**) Three-dimensional snapshots of the $ZnSO_4$ electrolyte with CNCs were obtained from MD simulations and partially enlarged snapshots for the solvation structure of Zn^{2+}. Reproduced with permission from ref. [206]. Copyright 2024, Wiley.

Moreover, molecular-level simulations provide detailed understanding of additive mechanisms, such as preferential adsorption on specific crystal planes and disruption of hydrogen-bonding networks. Wu et al. demonstrated through DFT and MD in Figure 7g that cellulose nanocrystals exhibit strong electrostatic interactions with Zn^{2+}, replacing water molecules in the solvation sheath and reducing parasitic reactions [206]. Xie's group used a similar multi-technique approach to show that propylene carbonate participates in the solvation structure, decreasing water coordination and promoting uniform deposition [207]. Such insights are critical for designing additives that enhance interfacial kinetics and inhibit dendrite growth. Finite element simulations, often conducted using COMSOL Multiphysics, offer a mesoscale perspective on ion transport and deposition morphology. These models visualize ion concentration gradients and electric field distribution, illustrating how additive-induced solid-electrolyte interphases promote homogeneous zinc plating [208]. When integrated with quantum mechanical and atomistic simulations, FEM provides a comprehensive multiscale understanding of electrolyte behavior, bridging atomic interactions with macroscopic performance.

In summary, the concerted application of theoretical and computational methods, spanning electronic structure calculations, classical and machine-learned potentials, and continuum modeling, has profoundly advanced the rational design of electrolyte additives for high-performance, dendrite-free zinc-ion batteries.

6. Conclusions and Outlook

6.1. Conclusions

This review has systematically examined the pivotal role of theoretical computational methods in advancing the understanding and development of ARZIBs. The main conclusions are shown as follows:

(1) Computational methodologies: A suite of computational techniques, including density functional theory (DFT), molecular dynamics (MD), monte carlo simulations, finite element method (FEM), machine learning (ML), and multiscale modeling, has been established as indispensable. Each method offers unique capabilities for probing ARZIB components across different spatial and temporal scales, from electronic structures to macroscopic device behavior, while also presenting specific limitations regarding computational cost, accuracy, and scale.

(2) Cathode material design: Theoretical calculations, particularly DFT and ab initio MD (AIMD), have provided profound atomic-level insights. They have been crucial in elucidating Zn^{2+} storage mechanisms, ion diffusion pathways, and the impact of strategic modifications such as doping, defect engineering (e.g., oxygen vacancies), and interlayer engineering in various cathode materials, including manganese-based and vanadium-based oxides, metal nitrides, phosphides, sulfides, selenides, Prussian blue analogues, and organic compounds. Computational studies have successfully decoded structure-property relationships, guiding the rational design of high-capacity and stable cathodes.

(3) Zinc anode stabilization: Computational studies have been instrumental in unraveling the fundamental mechanisms behind zinc dendrite formation, parasitic reactions (e.g., hydrogen evolution), and interfacial instability. DFT analyses of adsorption energetics and MD simulations of ion transport have identified key descriptors for ideal interface layers. Furthermore, FEM simulations have visualized the critical influence of electric field and ion concentration distribution on deposition homogeneity, providing a theoretical basis for designing protective layers and host structures for highly reversible zinc anodes.

(4) Electrolyte and interface engineering: At the electrolyte level, MD simulations and DFT calculations have revealed the intricate solvation structures of Zn^{2+} ions, the dynamics of hydrogen-bonding networks, and the specific interactions between functional groups, polymer chains, and electrode interfaces. This has enabled the rational design of hydrogel electrolytes and molecular additives that effectively suppress water activity, facilitate desolvation, and promote uniform zinc plating, thereby enhancing interfacial stability and cycling lifespan.

(5) Synergistic multi-scale and data-driven integration: The integration of multi-scale modeling frameworks is emerging as a powerful approach to bridge fundamental mechanisms with macroscopic performance.

Concurrently, the incorporation of machine learning and high-throughput computational screening is dramatically accelerating the discovery and optimization of novel materials and electrolytes, heralding a new paradigm for the rapid development of next-generation ARZIBs.

In summary, computational studies have transitioned from providing post-hoc explanations to playing a predictive and guiding role in the rational design of high-performance ARZIBs, offering invaluable insights that are often challenging to obtain solely through experimental approaches.

6.2. Outlook

Despite the significant progress enabled by theoretical computational methods in advancing ARZIBs, several challenges remain that must be addressed to fully realize their potential. Computational approaches, while powerful, are often constrained by the accuracy of force fields, the scalability of models, and the integration of multi-physics phenomena across different time and length scales. For instance, DFT calculations, though highly informative for electronic structure and ion diffusion properties, are limited by their high computational cost and inherent approximations, such as the choice of exchange-correlation functionals, which can affect the prediction of redox potentials and reaction barriers. Similarly, MD simulations rely heavily on the quality of force fields, which may not fully capture complex solvation structures or interfacial dynamics, especially under non-equilibrium conditions. Another major challenge lies in the accurate coupling of different computational techniques to form a cohesive multi-scale modeling framework. While efforts have been made to integrate quantum mechanics with continuum models, the transfer of parameters across scales often introduces uncertainties. Machine learning has emerged as a promising tool to bridge these gaps, yet it requires large, high-quality datasets that are often scarce in battery research. Moreover, the interpretability and physical consistency of ML models remain a concern, particularly when extrapolating beyond training data.

Future research should focus on developing more accurate and efficient computational methods tailored for ARZIBs. This includes the design of improved force fields for MD simulations, the incorporation of machine-learned potentials, and the advancement of hybrid quantum-classical methods to better describe electrochemical interfaces. Additionally, the integration of real-time data from operando experiments into computational models can enhance predictive accuracy and provide deeper insights into dynamic processes such as dendrite growth, phase transformation, and interfacial degradation. The application of artificial intelligence and high-throughput screening will accelerate the discovery of novel materials and electrolytes. However, these approaches must be coupled with robust validation experiments to ensure practical relevance. Furthermore, sustainability considerations should be incorporated into computational designs, such as minimizing the use of critical raw materials and optimizing battery lifecycle performance.

In conclusion, while computational methods have a profound impact on the understanding and design of ARZIBs, continued innovation in modeling techniques, coupled with closer integration with experimental studies, will be essential to overcome existing challenges and achieve the high performance, safety, and sustainability required for next-generation energy storage systems.

Author Contributions

Y.L.: conceptualization, writing—original draft preparation; Y.Y.: investigation, writing—original draft preparation; R.W.: writing—original draft preparation; L.D.: writing—original draft preparation; R.L.: writing—reviewing and editing; Y.C.: visualization, writing—reviewing and editing; H.W.: visualization, writing—reviewing and editing; X.Y.: writing—reviewing and editing; R.X.: supervision, writing—reviewing and editing; R.H.: supervision, writing—reviewing and editing. All authors have read and agreed to the published version of the manuscript.

Funding

This research was funded by Jiangsu Natural Science Foundation Youth Fund Project (No. BK20220700), Jiangsu Province Industry University Research Cooperation Project (No. BY20221063), Project of Natural Science Research in Colleges and Universities of Jiangsu Province (Nos. 21KJD150004), Jiangsu Province Education Department Major Project (Nos. 19KJA140003 and 21KJA530004), and Key R&D Plan (Social Development) Project of Yancheng Science and Technology Bureau (No. YCBE202243).

Institutional Review Board Statement

Not applicable.

Informed Consent Statement

Not applicable.

Data Availability Statement

The data supporting this review article can be obtained from authors or references.

Conflicts of Interest

The authors declare no conflict of interest.

Use of AI and AI-Assisted Technologies

No AI tools were utilized for this paper.

References

1. Zhou, W.; Tang, Y.; Zhang, X.; et al. MOF derived metal oxide composites and their applications in energy storage. *Coordin. Chem. Rev.* **2023**, *477*, 214949.
2. Kang, Z.; Zhao, Y.; Yang, D. Review of oil shale in-situ conversion technology. *Appl. Energy* **2020**, *269*, 115121.
3. Liu, Y.; Qian, J.; Shi, Y.; et al. Latest advances of metal-organic frameworks-based materials for supercapacitors. *Sustain. Mater. Techno.* **2023**, *36*, e00588.
4. Yang, S.; Cheng, Y.; Xiao, X.; et al. Development and application of carbon fiber in batteries. *Chem. Eng. J.* **2020**, *384*, 123294.
5. Xiao, X.; Zou, L.; Pang, H.; et al. Synthesis of micro/nanoscaled metal-organic frameworks and their direct electrochemical applications. *Chem. Soc. Rev.* **2020**, *49*, 301.
6. Ma, W.; Zhang, Y.; Pan, S.; et al. Smart fibers for energy conversion and storage. *Chem. Soc. Rev.* **2021**, *50*, 7009.
7. Yang, Y.; Hoang, M.T.; Bhardwaj, A.; et al. Perovskite solar cells based self-charging power packs: Fundamentals, applications and challenges. *Nano Energy* **2022**, *94*, 106910.
8. Yu, F.; Wang, Y.; Liu, Y.; et al. An aqueous rechargeable zinc-ion battery on basis of an organic pigment. *Rare Met.* **2022**, *41*, 2230.
9. Peng, Y.; Xu, J.; Xu, J.M.; et al. Metal-organic framework (MOF) composites as promising materials for energy storage applications. *Adv. Colloid Interf.* **2022**, *307*, 102732.
10. Xu, Y.; Li, Q.; Pang, H. Recent advances in metal organic frameworks and their composites for batteries. *Nano Futures* **2020**, *4*, 032007.
11. Luo, Y.; Tang, Y.; Zheng, S.; et al. Dual anode materials for lithium- and sodium-ion batteries. *J. Mater. Chem. A* **2018**, *6*, 4236.
12. Chi, C.; Liu, Z.; Lu, X.; et al. Balance of sulfur doping content and conductivity of hard carbon anode for high-performance K-ion storage. *Energy Storage Mater.* **2023**, *54*, 668.
13. Wang, Q.; Liu, Y.; Chen, P. Phenazine-based organic cathode for aqueous zinc secondary batteries. *J. Power Sources* **2020**, *468*, 228401.
14. Lv, T.; Peng, Y.; Zhang, G.; et al. How about vanadium-based compounds as cathode materials for aqueous zinc ion batteries. *Adv. Sci.* **2023**, *10*, 2206907.
15. Zhang, X.; Zhang, H.; Chen, M.; et al. Zinc-based fiber-shaped rechargeable batteries: Insights into structures, electrodes, and electrolytes. *Nano Res.* **2025**, *18*, 94907025.
16. Liu, Y.; Zhi, J.; Hoang, T.K.A.; et al. Paraffin based cathode-electrolyte interface for highly reversible aqueous zinc-ion battery. *ACS Appl. Energy Mater.* **2022**, *5*, 4840.
17. Wang, Q.; Liu, Y.; Wang, C.; et al. Vat orange 7 as an organic electrode with ultrafast hydronium-ion storage and super-long life for rechargeable aqueous zinc batteries. *Chem. Eng. J.* **2023**, *451*, 138776.
18. Hariprakash, B.; Martha, S.; Ambalavanan, S.; et al. Comparative study of lead-acid batteries for photovoltaic stand-alone lighting systems. *J. Appl. Electrochem.* **2008**, *38*, 77.
19. Liu, Y.; Wen, Z.; Wu, X.; et al. Holze. An acid-free rechargeable battery based on $PbSO_4$ and spinel $LiMn_2O_4$. *Chem. Commun.* **2014**, *50*, 13714.
20. Wang, H.; Liang, Y.; Gong, M.; et al. An ultrafast nickel-iron battery from strongly coupled inorganic nanoparticle/nanocarbon hybrid materials. *Nat. Commun.* **2012**, *3*, 917.
21. Liu, Y.; Xie, D.; Shi, Y.; et al. An aqueous rechargeable Fe//$LiMn_2O_4$ hybrid battery with superior electrochemical performance beyond mainstream Fe-based batteries. *Nano Res.* **2024**, *17*, 5168.
22. Sun, Y.; Liu, Y.; Han, Y.; et al. Effects of thermal transformation on graphene-like lamellar porous carbon and surface-contributed capacitance. *Mater. Today Commun.* **2021**, *29*, 102982.

23. Liu, Y.; Xu, Y.; Chang, Y.; et al. A new high-current electrochemical capacitor using MnO_2-coated vapor-grown carbon fibers. *Crystals* **2022**, *12*, 1444.
24. Baig, M.M.; Khan, S.A.; Ahmad, H.; et al. 3D printing of hydrogels for flexible micro-supercapacitors. *FlexMat* **2024**, *1*, 79.
25. Zhu, G.; Hou, Y.; Lu, J.; et al. MXene decorated 3D-printed carbon black-based electrodes for solid-state micro-supercapacitors. *J. Mater. Chem. A* **2023**, *11*, 25422.
26. Liu, Y.; Zhang, B.; Wang, F.; et al. Nanostructured intercalation compounds as cathode materials for supercapacitors. *Pure Appl. Chem.* **2014**, *86*, 593.
27. Zhang, Y.; Li, Q.; Feng, W.; et al. Valence engineering via polyoxometalate-induced on vanadium centers for efficient aqueous zinc-ion batteries. *Angew. Chem. Int. Ed.* **2025**, *137*, e202501728.
28. Liu, Y.; Zhi, J.; Sedighi, M.; et al. Mn^{2+} ions confined by electrode microskin for aqueous battery beyond intercalation capacity. *Adv. Energy Mater.* **2020**, *10*, 2002578.
29. Hu, Q.; Hu, J.; Ma, F.; et al. Redistributing zinc-ion flux by work function chemistry toward stabilized and durable Zn metal batteries. *Energy Environ. Sci.* **2024**, *17*, 2554.
30. Liu, Y.; Shi, Q.; Wu, Y.; et al. Highly efficient dendrite suppressor and corrosion inhibitor based on gelatin/Mn^{2+} co-additives for aqueous rechargeable zinc-manganese dioxide battery. *Chem. Eng. J.* **2021**, *407*, 127189.
31. Zhang, Y.; Li, X.; Fan, L.; et al. Ultrathin and super-rough membrane for anti-dendrite separator in aqueous zinc-ion batteries. *Cell Rep. Phys. Sci.* **2022**, *3*, 100824.
32. Yang, X.; Wu, W.; Liu, Y.; et al. Chitosan modified filter paper separators with specific ion adsorption to inhibit side reactions and induce uniform Zn deposition for aqueous Zn batteries. *Chem. Eng. J.* **2022**, *450*, 137902.
33. Li, H.; Yang, G.; Chen, J.; et al. Revealing the electrochemistry in a voltaic cell by in situ electron microscopy. *ChemElectroChem* **2022**, *9*, e202200441.
34. Dong, X.; Wang, Y.; Xia, Y. Re-building daniell cell with a Li-ion exchange film. *Sci. Rep.* **2014**, *4*, 6916.
35. Wruck, W.J.; Reichman, B.; Bullock, K.R.; et al. Rechargeable Zn-MnO_2 alkaline batteries. *J. Electrochem. Soc.* **1991**, *138*, 3560.
36. Pan, J.; Xu, Y.Y.; Yang, H.; et al. Advanced architectures and relatives of air electrodes in Zn–air batteries. *Adv. Sci.* **2018**, *5*, 1700691.
37. Han, M.; Chen, D.; Lu, Q.; et al. Aqueous rechargeable Zn–iodine batteries: Issues, strategies and perspectives. *Small* **2024**, *20*, 2310293.
38. Mahmood, A.; Zheng, Z.; Zinc, Y.C. Zinc–bromine batteries: Challenges, prospective solutions, and future. *Adv. Sci.* **2024**, *11*, 2305561.
39. Lu, H.; Hu, J.; Zhang, K.; et al. Microfluidic-assisted 3D printing zinc powder anode with 2D conductive MOF/MXene heterostructures for high-stable zinc−organic battery. *Adv. Mater.* **2024**, *36*, 2309753.
40. Lu, J.; Wang, T.; Yang, J.; et al. Multifunctional self-assembled bio-interfacial layers for high-performance zinc metal anodes. *Angew. Chem. Int. Ed.* **2024**, *63*, e202409838.
41. Ding, X.; Jia, X.; Yuan, H.; et al. Tumor microenvironment–activated Zn//MnO_2 battery for sustained and local electrochemical immunotherapy. *Sci. Adv.* **2025**, *11*, eadu1647.
42. Brunk, E.; Ursula, R. Mixed quantum mechanical/molecular mechanical molecular dynamics simulations of biological systems in ground and electronically excited states. *Chem. Rev.* **2015**, *115*, 6217.
43. Song, L.; De, N.; Yan, C.; et al. Correlating solid electrolyte interphase composition with dendrite-free and long life-span lithium metal batteries via advanced characterizations and simulations. *Small Methods* **2023**, *7*, 2300168.
44. Tian, M.; Wang, Z.; Yang, H.Y.; et al. Recent progress in computational materials science boosting development of rechargeable batteries. *Adv. Energy Mater.* **2025**, *15*, 2403443.
45. Yan, L.; Su, J.; Sun, C.; et al. Review of the first principles calculations and the design of cathode materials for Li-ion batteries. *Adv. Manuf.* **2014**, *2*, 358.
46. Markov, I.L. Limits on fundamental limits to computation. *Nature* **2014**, *512*, 147.
47. Tuckerman, M.E.; Martyna, G.J. Understanding modern molecular dynamics: Techniques and applications. *J. Phys. Chem. B* **2000**, *104*, 159.
48. Yamakov, V.; Wolf, D.; Phillpot, S.R.; et al. Deformation-mechanism map for nanocrystalline metals by molecular-dynamics simulation. *Nat. Mater.* **2004**, *3*, 43.
49. van Gunsteren, W.F.; Oostenbrink, C. Methods for classical-mechanical molecular simulation in chemistry: Achievements, limitations, perspectives. *J. Chem. Inf. Model.* **2024**, *64*, 6281.
50. Gavilán-Arriazu, E.M.; Mercer, M.P.; Barraco, D.E.; et al. Kinetic monte carlo simulations applied to Li-ion and post Li-ion batteries: A key link in the multi-scale chain. *Prog. Energy* **2021**, *3*, 042001.
51. Wu, S.; Chen, Y.; Luan, W.; et al. A review of multiscale mechanical failures in lithium-ion batteries: Implications for performance, lifetime and safety. *Electrochem. Energy Rev.* **2024**, *7*, 35.

52. Zhang, J. Modern monte carlo methods for efficient uncertainty quantification and propagation: A survey. *Wires. Comput. Stat.* **2021**, *13*, e1539.
53. Zuo, S.; Yin, B.; Xu, Y.; et al. A simplified method of soft connected battery module for finite element method model of battery pack. *Int. J. Energy Res.* **2021**, *45*, 10546.
54. Song, S.; Zhu, M.; Xiong, Y.; et al. Mechanical failure mechanism of silicon-based composite anodes under overdischarging conditions based on finite element analysis. *ACS Appl. Mater. Interfaces* **2021**, *13*, 34157.
55. Liu, Y.; Zheng, G.; Letov, N.; et al. A survey of modeling and optimization methods for multi-scale heterogeneous lattice structures. *J. Mechan. Des.* **2021**, *143*, 040803.
56. Kotsiantis, S.B.; Zaharakis, I.D.; Pintelas, P.E. Machine learning: A review of classification and combining techniques. *Artif. Intell. Rev.* **2006**, *26*, 159.
57. Nozarijouybari, Z.; Fathy, H.K. Machine learning for battery systems applications: Progress, challenges, and opportunities. *J. Power Sources* **2024**, *601*, 234272.
58. Nair, M.R.; Roy, T. Role of artificial intelligence in the design and discovery of next-generation battery electrolytes. *Chem. Phys. Rev.* **2025**, *6*, 011311.
59. Roman, D.; Saxena, S.; Robu, V.; et al. Machine learning pipeline for battery state-of-health estimation. *Nat. Mach. Intell.* **2021**, *3*, 447.
60. Parmar, J.; Chouhan, S.; Raychoudhury, V.; et al. Open-world machine learning: Applications, challenges, and opportunities. *ACM Comput. Surv.* **2023**, *55*, 1–37.
61. Liu, X.; Zhang, L.; Yu, H.; et al. Bridging multiscale characterization technologies and digital modeling to evaluate lithium battery full lifecycle. *Adv. Energy Mater.* **2022**, *12*, 2200889.
62. Chen, X.; Liu, X.; Shen, X.; et al. Applying machine learning to rechargeable batteries: From the microscale to the macroscale. *Angew. Chem. Int. Ed.* **2021**, *133*, 24558.
63. de Carvalho, F.O.; Sousa, O.; Assali, L.V.C.; et al. Accelerating Cathode design for zinc-ion batteries using data-driven screening and ab initio calculations. *J. Mater. Chem. A* **2025**, *13*, 29317–29322. https://doi.org/10.1039/D5TA02667A.
64. Li, G.; Sun, L.; Zhang, S; et al. Developing cathode materials for aqueous zinc ion batteries: Challenges and practical prospects. *Adv. Funct. Mater.* **2024**, *34*, 2301291.
65. Cao, H.; Zheng, Z.; Norby, P.; et al. Electrochemically induced phase transition in V3O7·H2O nanobelts/reduced graphene oxide composites for aqueous zinc-ion batteries. *Small* **2021**, *17*, 2100558.
66. Chen, S.; Kong, Y.; Tang, C.; et al. Doping regulation stabilizing δ-MnO_2 cathode for high-performance aqueous aluminum-ion batteries. *Small* **2024**, *20*, 2312229.
67. Liang, J.; Zhao, Y.; Ren, L.; et al. Dual anions doping enhanced conductivity and stability of layered δ-MnO2 cathode for aqueous zinc-ion battery. *Adv. Funct. Mater.* **2025**, *35*, 2501135.
68. Wang, S.; Yao, S.; Dai, N.; et al. Spin symmetry breaking-induced hubbard gap near-closure in N-coordinated MnO2 for enhanced aqueous zinc-ion battery performance. *Angew. Chem. Int. Ed.* **2024**, *63*, e202408414.
69. Chao, D.; Ye, C.; Xie, F.; et al. Atomic engineering catalyzed MnO_2 electrolysis kinetics for a hybrid aqueous battery with high power and energy density. *Adv. Mater.* **2020**, *32*, 2001894.
70. Nam, K.W.; Kim, H.; Choi, J.H.; et al. Crystal water for high performance layered manganese oxide cathodes in aqueous rechargeable zinc batteries. *Energy Environ. Sci.* **2019**, *12*, 1999.
71. Chen, H.; Ruan, P.; Zhang, H.; et al. Achieving highly reversible Mn^{2+}/MnO_2 conversion reaction in electrolytic Zn-MnO2 batteries via electrochemical-chemical process regulation. *Angew. Chem. Int. Ed.* **2025**, *64*, e202423999.
72. Chen, N.; Wang, W.; Ma, Y.; et al. Aqueous zinc-chlorine battery modulated by a MnO_2 redox adsorbent. *Small Methods* **2023**, *8*, 2201553.
73. Chen, C.; Shi, M.; Zhao, Y.; et al. Al-intercalated MnO_2 cathode with reversible phase transition for aqueous Zn-ion batteries. *Chem. Eng. J.* **2021**, *422*, 130375.
74. Li, X.; Zhou, Q.; Yang, Z.; et al. Unraveling the role of nitrogen-doped carbon nanowires incorporated with MnO_2 nanosheets as high performance cathode for zinc-ion batteries. *Energy Environ. Mater.* **2022**, *6*, e12378.
75. Zheng, W.; Cui, Z.; Liu, C.; et al. Tailoring hierarchical MnO_2 nanostructures on self-supporting cathodes for high-mass-loading zinc-ion batteries. *Chem. Sci.* **2024**, *15*, 20303.
76. Li, M.; Liu, C.; Meng, J.; et al. Hydroxylated manganese oxide cathode for stable aqueous zinc-ion batteries. *Adv. Funct. Mater.* **2024**, *34*, 2405659.
77. Xu, N.; Zhang, Y.; Wang, M.; et al. High-performing rechargeable/flexible zinc-air batteries by coordinated hierarchical Bi-metallic electrocatalyst and heterostructure anion exchange membrane. *Nano Energy* **2019**, *65*, 104021.
78. Le, T.; Takeuchi, E.S.; Takeuchi, K.J.; et al. Tuning discharge behavior of hollandite α-MnO_2 in hydrated zinc ion battery by transition metal substitution. *J. Phys. Chem. C* **2023**, *127*, 907.
79. Jiang, H.; Gong, W.; Zhang, Y.; et al. Quench-tailored Al-doped V_2O_5 nanomaterials for efficient aqueous zinc-ion batteries. *J. Energy Chem.* **2022**, *70*, 52.

80. Liu, Y.; Lu, C.; Yang, Y.; et al. Multiple cations nanoconfinement in ultrathin V_2O_5 nanosheets enables ultrafast ion diffusion kinetics toward high-performance zinc ion battery. *Adv. Mater.* **2024**, *36*, 2312982.
81. Wang, W.; Zhang, L.; Duan, Z.; et al. Joint cationic and anionic redox chemistry in a vanadium oxide cathode for zinc batteries achieving high energy density. *Carbon Energy* **2024**, *6*, e577.
82. Xu, X.; Qian, Y.; Wang, C.; et al. Enhanced charge transfer and reaction kinetics of vanadium pentoxide for zinc storage via nitrogen interstitial doping. *Chem. Eng. J.* **2023**, *451*, 138770.
83. Zhang, B.; Han, X.; Kang, W.; et al. Structure and oxygen-defect regulation of hydrated vanadium oxide for enhanced zinc ion storage via interlayer doping strategy. *Nano Res.* **2023**, *16*, 6094.
84. Zhang, Y.; Li, Z.; Liu, M.; et al. Construction of novel polyaniline-intercalated hierarchical porous V_2O_5 nanobelts with enhanced diffusion kinetics and ultra-stable cyclability for aqueous zinc-ion batteries. *Chem. Eng. J.* **2023**, *463*, 142425.
85. Pan, R.; Zheng, A.; He, B.; et al. In situ crafting of a 3D N-doped carbon/defect-rich V2O5-xnH2O nanosheet composite for high performance fibrous flexible Zn-ion batteries. *Nanoscale Horiz.* **2022**, *7*, 1501.
86. Wu, T.; Zhu, K.; Qin, C.; et al. Unraveling the role of structural water in bilayer V_2O_5 during Zn^{2+}-intercalation: Insights from DFT calculations. *J. Mater. Chem. A* **2019**, *7*, 5612.
87. Wang, Z.; Liang, P.; Zhang, R.; et al. Oxygen-defective V_2O_5 nanosheets boosting 3D diffusion and reversible storage of zinc ion for aqueous zinc-ion batteries. *Appl. Surf. Sci.* **2021**, *562*, 150196.
88. Chen, J.; Zhang, W.; Zhang, X.; et al. Sodium pre-intercalated carbon/V_2O_5 constructed by sustainable sodium lignosulfonate for stable cathodes in zinc ion batteries: A comprehensive study. *ChemSusChem* **2022**, *15*, e202200732.
89. Wang, Y.; Wei, S.; Qi, Z.; et al. Intercalant-induced V t2g orbital occupation in vanadium oxide cathode toward fast-charging aqueous zinc-ion batteries. *Proc. Natl. Acad. Sci. USA* **2023**, *120*, e2217208120.
90. Deng, W.; Li, C.; Zou, W.; et al. Understanding the super-theoretical capacity behavior of VO2 in aqueous Zn batteries. *Small* **2023**, *20*, 2309527.
91. Wang, Z.; Cui, P.; Wang, X.; et al. Co-substitution engineering boosting the kinetics and stability of VO_2 for Zn ion batteries. *Adv. Funct. Mater.* **2024**, *34*, 2407925.
92. Li, Z.; Ren, Y.; Mo, L.; et al. Impacts of oxygen vacancies on zinc ion intercalation in VO_2. *ACS Nano* **2020**, *14*, 5581.
93. Luo, H.; Wang, B.; Wang, C.; et al. Synergistic deficiency and heterojunction engineering boosted VO_2 redox kinetics for aqueous zinc-ion batteries with superior comprehensive performance. *Energy Storage Mater.* **2020**, *33*, 390.
94. Luo, P.; Zhang, W.; Cai, W.; et al. Accelerated ion/electron transport kinetics and increased active sites via local internal electric fields in heterostructured VO_2-carbon cloth for enhanced zinc-ion storage. *Nano Res.* **2023**, *16*, 503.
95. Zhang, W.; Liu, J.; Cai, W.; et al. An. Engineering d-p orbital hybridization through regulation of interband energy separation for durable aqueous Zn//VO_2(B) batteries. *Chem. Eng. J.* **2023**, *464*, 142711.
96. Guan, K.; Duan, K.; Yang, G.; et al. Ultra-long cycle H-doped VO_2(B) cathode for high capacity aqueous Zn-ion battery. *Mater. Today Adv.* **2022**, *14*, 100230.
97. Liu, W.; Zong, H.; Li, M.; et al. Ta4C3 modulated MOF-derived 3D crosslinking network of VO_2(B)@Ta_4C_3 for high-performance aqueous zinc ion batteries. *ACS Appl. Mater. Interfaces* **2023**, *15*, 13554.
98. Zhang, L.; Fang, D.; Wang, F.; et al. nterlayer and O-vacancy engineering co-boosting fast kinetics and stable structure of hydrated sodium ammonium vanadate for aqueous zinc-ion battery. *Chem. Eng. J.* **2025**, *506*, 159920.
99. Cui, F.; Wang, D.; Hu, F.; et al. Deficiency and surface engineering boosting electronic and ionic kinetics in NH4V4O10 for high-performance aqueous zinc-ion battery. *Energy Storage Mater.* **2022**, *44*, 197.
100. Li, M.; Zhang, Y.; Hu, J.; et al. Universal multifunctional hydrogen bond network construction strategy for enhanced aqueous Zn^{2+}/proton hybrid batteries. *Nano Energy* **2022**, *100*, 107539.
101. Liu, Y.; Lv, J.; Cao, T.; et al. Unsaturated Ni/V centers and short Ni·V/Ni distances in nickel vanadate for high-performance zinc-ion battery. *Chem. Eng. J.* **2022**, *441*, 136007.
102. Wang, S.; Cao, Y.; Qin, J.; et al. Revealing the self-generated heterointerface of NaV_2O_5 in Zn storage via a scalable production method. *ACS Sustain. Chem. Eng.* **2023**, *11*, 6710.
103. Zang, Q.; Cheng, X.; Chen, S.; et al. Oxygen defect engineering triggered by S-doping boosts the performance of H2V3O8 nanobelts for aqueous Zn-ion storage. *Chem. Eng. J.* **2023**, *452*, 139396.
104. Cao, H.; Peng, C.; Zheng, Z.; et al. Orientation effect of zinc vanadate cathode on zinc ion storage performance. *Electrochim. Acta* **2021**, *388*, 138646.
105. Liu, C.; Liu, Y.; Liu, X.; et al. Coordination polymer-derived Al^{3+}-doped V_2O_3/C with rich oxygen vacancies for an advanced aqueous zinc-ion battery with ultrahigh rate capability. *Sustain. Energy Fuels* **2022**, *6*, 2020.
106. Bai, Y.; Zhang, H.; Xiang, B.; et al. Oxygen vacancy-rich, binder-free copper pyrovanadate for zinc ion storage. *Chem. Eng. J.* **2021**, *420*, 130474.
107. Li, Q.; Zhang, Q.; Zhou, Z.; et al. Boosting Zn-ion storage capability of self-standing Zn-doped Co_3O_4 nanowire array as advanced cathodes for high-performance wearable aqueous rechargeable Co//Zn batteries. *Nano Res.* **2021**, *14*, 91.

108. Long, J.; Gu, J.; Yang, Z.; et al. Highly porous, low band-gap $Ni_xMn_{3x}O_4$ ($0.55 < x < 1.2$) spinel nanoparticles with in situ coated carbon as advanced cathode materials for zinc-ion batteries. *J. Mater. Chem. A* **2019**, *7*, 17854.
109. Mallick, S.; Choutipalli, V.S.K.; Bag, S.; et al. Defect engineered ternary spinel: An efficient cathode for an aqueous rechargeable zinc-ion battery of long-term cyclability. *ACS Appl. Mater. Interfaces* **2022**, *14*, 37577.
110. Shao, T.; Zhang, Y.; Cao, T.; et al. Structural regulation of $ZnMn_2O_4$ cathode material by K, Fe-double doping to improve its rate and cycling stability for rechargeable aqueous zinc-based batteries. *Chem. Eng. J.* **2022**, *431*, 133735.
111. Tan, Y.; He, J.; Wang, B.; et al. Tuning the layer structure of molybdenum trioxide towards high-performance aqueous zinc-ion batteries. *Chin. Chem. Lett.* **2023**, *34*, 107410.
112. Teng, C.; Yang, F.; Sun, M.; et al. Structural and defect engineering of cobaltosic oxide nanoarchitectures as an ultrahigh energy density and super durable cathode for Zn-based batteries. *Chem. Sci.* **2019**, *10*, 7600.
113. Wang, K.; Guo, G.; Tan, X.; et al. Achieving high-energy and long-cycling aqueous zinc-metal batteries by highly reversible insertion mechanisms in Ti-substituted $Na_{0.44}MnO_2$ cathode. *Chem. Eng. J.* **2023**, *451*, 139059.
114. Wei, J.; Guo, J.; Wang, S.; et al. Fabrication of dual-functional electrodes using oxygen vacancy abundant $NiCo_2O_4$ nanosheets for advanced hybrid supercapacitors and Zn-ion batteries. *Inorg. Chem. Front.* **2022**, *9*, 4452.
115. Zhang, Y.; Xu, J.; Liu, C.; et al. Ion-exchange-induced high-performance of inverse spinel Mg2VO4 for aqueous zinc-ion batteries. *J. Power Sources* **2022**, *549*, 232075.
116. Bai, Y.; Luo, L.; Song, W.; et al. Nitrogen-vacancy-rich VN clusters embedded in carbon matrix for high-performance zinc ion batteries. *Adv. Sci.* **2024**, *11*, 2308668.
117. Bian, Y.; Hu, R.; Wang, H.; et al. Developing an in situ polyoxovanadate to vanadium nitride/carbon conversion strategies in manufacture aqueous zinc ion batteries cathode with ultrahigh rate capability. *Adv. Funct. Mater.* **2024**, *35*, 2418671.
118. Chen, J.; Guo, K.; Ren, T.; et al. Aluminium-doped vanadium nitride as cathode material for high-performance aqueous zinc-ion batteries. *J. Power Sources* **2025**, *626*, 235751.
119. Dai, Y.; Lu, R.; Zhang, C.; et al. Zn^{2+}-mediated catalysis for fast-charging aqueous Zn-ion batteries. *Nat. Catal.* **2024**, *7*, 776.
120. Luo, S.; Cui, J.; Liang, S.; et al. Carbon-enveloped pea-shaped vanadium nitride nanorods for aqueous zinc ion batteries. *J. Mater. Chem. C* **2024**, *12*, 6153.
121. Posadzy, M.; Garcia-Rodriguez, M.; Flores-Lasluisa, J.X.; et al. High-performance transition metal nitride/carbon nanofiber composites as positive electrode in rechargeable Zn-air batteries. *Carbon* **2025**, *239*, 120308.
122. Yao, X.; Khanam, Z.; Li, C.; et al. Unlatching the additional zinc storage ability of vanadium nitride nanocrystallites. *Small* **2024**, *20*, 2312036.
123. Wang, H.; Hou, W.; Wang, X.; et al. Construction of MOF-derived vanadium nitride decorated micro/mesoporous carbon nanofibers for aqueous zinc-ion batteries. *Chem. Eur. J.* **2025**, *31*, e202403903.
124. Chen, D.; Lu, M.; Wang, B.; et al. Uncover the mystery of high-performance aqueous zinc-ion batteries constructed by oxygen-doped vanadium nitride cathode: Cationic conversion reaction works. *Energy Storage Mater.* **2021**, *35*, 679.
125. Jung, H.; Lee, J.; Park, J.; et al. A mesoporous tungsten oxynitride nanoffbers/graphite felt composite electrode with high catalytic activity for the cathode in Zn-Br flow battery. *Small* **2023**, *19*, 2208280.
126. Dong, C.; Tang, S.; Chen, Y.; et al. Identifying the synergistic Na^+/Zn^{2+} cointercalation mechanism for boosting electrochemical performance of $Na_4Fe_3(PO_4)_2P_2O_7$ in Zn-ion batteries. *ACS Mater. Lett.* **2023**, *5*, 1170.
127. Hu, L.; Wu, Z.; Lu, C.; et al. Principles of interlayer-spacing regulation of layered vanadium phosphates for superior zinc-ion batteries. *Energy Environ. Sci.* **2021**, *14*, 4095.
128. Wu, Z.; Lu, C.; Ye, F.; et al. Bilayered $VOPO_4{\cdot}2H_2O$ nanosheets with high-concentration oxygen vacancies for high-performance aqueous zinc-ion batteries. *Adv. Funct. Mater.* **2021**, *31*, 2106816.
129. Zhao, S.; Qu, G.; Wang, C.; et al. Towards advanced aqueous zinc battery by exploiting synergistic effects between crystalline phosphide and amorphous phosphate. *Nanoscale* **2021**, *13*, 18586.
130. Zhao, D.; Chen, S.; Lai, Y.; et al. A stable "rocking-chair" zinc-ion battery boosted by low-strain $Zn_3V_4(PO_4)_6$ cathode. *Nano Energy* **2022**, *100*, 107520.
131. Chen, L.; Gao, X.; Nie, H.; et al. Electrochemical oxidation endows VN/V_3S_4 heterostructure with high performance in aqueous zinc-ion batteries. *J. Alloy. Compd.* **2023**, *958*, 170491.
132. Li, X.; Zhao, S.; Qu, G.; et al. Defect engineering in Co-doped Ni_3S_2 nanosheets as cathode for high-performance aqueous zinc ion battery. *J. Mater. Sci. Techn.* **2022**, *118*, 190.
133. Tian, G.; Ling, D.; Chen, Z.; et al. Effective CuO/Cu_7S_4 nanospheres heterostructures for advanced "rocking-chair" zinc-ion battery. *J. Colloid Interf. Sci.* **2025**, *679*, 334.
134. Li, C.; Liu, C.; Wang, Y.; et al. Drastically-enlarged interlayer-spacing MoS_2 nanocages by inserted carbon motifs as high performance cathodes for aqueous zinc-ion batteries. *Energy Storage Mater.* **2022**, *49*, 144.
135. Liu, F.; Li, L.; Xu, S.; et al. Cobalt-doped $MoS_2{\cdot}nH_2O$ nanosheets induced heterogeneous phases as high-rate capability and long-term cyclability cathodes for wearable zinc-ion batteries. *Energy Storage Mater.* **2023**, *55*, 1–11.

136. Li, S.; Huang, C.; Gao, L.; et al. Unveiling the "proton lubricant" chemistry in aqueous zinc-MoS_2 batteries. *Angew. Chem. Int. Ed.* **2022**, *134*, e202211478.
137. Liu, L.; Yang, W.; Chen, H.; et al. High zinc-ion intercalation reaction activity of MoS_2 cathode based on regulation of thermodynamic metastability and interlayer water. *Electrochim. Acta* **2022**, *410*, 140016.
138. Liu, J.; Xu, P.; Liang, J.; et al. Boosting aqueous zinc-ion storage in MoS_2 via controllable phase. *Chem. Eng. J.* **2020**, *389*, 124405.
139. Mao, Y.; Bai, J.; Si, J.; et al. Magneto-electrochemistry driven ultralong-life Zn-VS_2 aqueous zinc-ion batteries. *Mater. Horiz.* **2023**, *10*, 3162.
140. Ren, Z.; Sun, Y.; Yin, Y.; et al. Metallic V_5S_8 microparticles with tunnel-like structure for high-rate and stable zinc-ion energy storage. *Energy Storage Mater.* **2021**, *42*, 786.
141. Tan, Y.; Li, S.; Zhao, X.; et al. Unexpected role of the interlayer "dead Zn^{2+}" in strengthening the nanostructures of VS_2 cathodes for high-performance aqueous Zn-ion storage. *Adv. Energy Mater.* **2022**, *12*, 2104001.
142. Wang, X.; Zhang, S.; Yang, R.; et al. Hierarchical carbon nanosheet confined defective MoSx cathode towards long-cycling zinc-ion-battery. *Nano Res.* **2023**, *16*, 9364.
143. Xu, H.; Yang, W.; Liu, H.; et al. Boosting kinetics of tellurium redox reaction for high-performance aqueous zinc-tellurium batteries. *Chem. Eng. J.* **2023**, *465*, 142896.
144. Yu, J.; Cai, D.; Si, J.; et al. MOF-derived $NiCo_2S_4$ and carbon hybrid hollow spheres compactly concatenated by electrospun carbon nanofibers as self-standing electrodes for aqueous alkaline Zn batteries. *J. Mater. Chem. A* **2022**, *10*, 4100.
145. Bai, Y.; Zhang, H.; Song, H.; et al. Engineering anion defects of ternary V-S-Se layered cathodes for ultrafast zinc ion storage. *Nano Energy* **2024**, *120*, 109090.
146. Chen, X.; Zhang, A.; Zou, H.; et al. Defect engineering modulated $MoSe_2$ cathode achieves highly effective photo-responsive zinc ion battery. *Energy Storage Mater.* **2024**, *70*, 103457.
147. Aghdam, A.M.; Habibzadeh, S.; Javanbakht, M.; et al. High interspace-layer manganese selenide nanorods as a high performance cathode for aqueous zinc-ion batteries. *ACS Appl. Energy Mater.* **2023**, *6*, 3225.
148. Wu, Z.; Lu, C.; Wang, Y.; et al. Ultrathin VSe_2 nanosheets with fast ion diffusion and robust structural stability for rechargeable zinc-ion battery cathode. *Small* **2020**, *16*, 2000698.
149. Cui, M.; Zhu, Y.; Lei, H.; et al. Anion–cation competition chemistry for comprehensive high performance prussian blue analogs cathodes. *Angew. Chem. Int. Ed.* **2024**, *63*, e202405428.
150. Fu, H.; Wang, X.; Ye, L.; et al. Optimizing Fe in Mn-based prussian blue analogs with dual redox-active sites to enhance operating voltage and durability in Zn-ion batteries. *Chem. Eng. J.* **2025**, *506*, 160308.
151. Li, W.; Hei, P.; Sai, Y.; et al. Vanadium-based prussian blue analogue for high energy aqueous zinc-iodine batteries. *Chem. Eng. J.* **2025**, *510*, 161720.
152. Puthiyaveetil, P.P.; Nair, A.; Dilwale, S.; et al. Insights on prussian blue analogue cathode material engineered with polypyrrole surface protection layer for aqueous rechargeable zinc metal battery. *Small* **2024**, *21*, 2409947.
153. Qian, Y.; Chang, G.; Huang, C.; et al. A transformed prussian blue analog as host of I2 for long-life aqueous zinc-iodine battery. *Chem. Eng. J.* **2025**, *503*, 158392.
154. Wang, L.; Liu, N.; Li, Q.; et al. Dual redox reactions of silver hexacyanoferrate prussian blue analogue enable superior electrochemical performance for zinc-ion storage. *Angew. Chem. Int. Ed.* **2025**, *137*, e202416392.
155. Gao, W.; Cheng, S.; Zhang, Y.; et al. Efficient charge storage in zinc–iodine batteries based on pre-embedded iodine-ions with reduced electrochemical reaction barrier and suppression of polyiodide self-shuttle effect. *Adv. Funct. Mater.* **2023**, *33*, 2211979.
156. Tan, Y.; Yang, H.; Miao, C.; et al. Hydroxylation strategy unlocking multi-redox reaction of manganese hexacyanoferrate for aqueous zinc-ion battery. *Chem. Eng. J.* **2023**, *457*, 141323.
157. Ding, C.; Zhao, Y.; Yin, W.; et al. Regulating intermolecular hydrogen bonds in organic cathode materials to realize ultra-stable, flexible and low-temperature aqueous zinc-organic batteries. *Angew. Chem. Int. Ed.* **2025**, *137*, e202417988.
158. Hong, H.; Wang, Y.; Wei, Z.; et al. Constructing a janus catholyte/cathode structure: A new strategy for stable Zn-organic batteries. *Adv. Mater.* **2024**, *36*, 2410209.
159. Hua, K.; Ma, Q.; Liu, Y.; et al. High-performance bipolar small-molecule organic cathode for wide-temperature range aqueous zinc-ion batteries. *ACS Nano* **2025**, *19*, 14249.
160. Li, C.; Hu, L.; Ren, X.; et al. Asymmetric charge distribution of active centers in small molecule quinone cathode boosts high-energy and high-rate aqueous Zinc-organic batteries. *Adv. Funct. Mater.* **2023**, *34*, 2313241.
161. Zhang, L.; Wang, X.; Wang, X.; et al. Electron-withdrawing group functionalization for improved zinc-ion storage in organic electrode materials. *Chem. Eng. J.* **2025**, *521*, 166985.
162. Zhang, Y.; Li, M.; Li, Z.; et al. A high capacity p-type organic cathode material for aqueous zinc batteries. *Angew. Chem.* **2024**, *136*, e202410342.

163. Kundu, D.; Oberholzer, P.; Glaros, C.; et al. An organic cathode for aqueous Zn batteries: Taming a unique phase evolution towards stable electrochemical cycling. *Chem. Mater.* **2018**, *30*, 3874.
164. Li, L.; Wang, Y.; Gong, W.; et al. Building stable small molecule imide cathodes toward ultralong-life aqueous zinc-organic batteries. *Chem. Eng. J.* **2023**, *465*, 142824.
165. Wang, Y.; Wang, X.; Tang, J.; et al. A quinoxalinophenazinedione covalent triazine framework for boosted high-performance aqueous zinc-ion batteries. *J. Mater. Chem. A* **2022**, *10*, 13868.
166. Wang, J.; Zhang, X.; Yan, Z.; et al. Tetrathiafulvalene as a sustainable cathode with high rate and long life-span for aqueous Zinc-ion battery at low temperatures. *Chem. Eng. J.* **2023**, *459*, 141649.
167. Ding, Y.; Cai, C.; Ma, L.; et al. Tailoring MnO_2 cathode interface via organic–inorganic hybridization engineering for ultra-stable aqueous zinc-ion batteries. *Adv. Energy Mater.* **2024**, *15*, 2402819.
168. Sang, B.; Wang, X.; Feng, K.; et al. Boosting zinc-ion storage performance by interlayer chemistry modulation on an organic-inorganic hybrid cathode. *J. Colloid Interf. Sci.* **2024**, *653*, 199.
169. Luo, Z.; Liu, Z.; He, H.; et al. Suppressing the dissolution of vanadium by organic-inorganic hybrid for aqueous zinc-ion batteries. *J. Mater. Sci. Techn.* **2023**, *145*, 93.
170. Ma, X.; Cao, X.; Yao, M.; et al. Organic–inorganic hybrid cathode with dual energy storage mechanism for ultrahigh-rate and ultralong-life aqueous zinc-ion batteries. *Adv. Mater.* **2022**, *34*, 2105452.
171. Nagarai, R.; Pakhira, S.; Aruchamy, K.; et al. Catalyzing the intercalation storage capacity of aqueous zinc-ion battery constructed with Zn(II) preinserted organo-vanadyl hybrid cathode. *ACS Appl. Energy Mater.* **2020**, *3*, 3425.
172. Sariyer, S.; Yesilot, S.; Kilic, N.; et al. Polyphosphazene based inorganic-organic hybrid cathode containing pyrene tetraone sides for aqueous zinc-ion batteries. *Batter. Supercaps* **2023**, *6*, e202200529.
173. Cao, J.; Wu, H.; Zhang, D.; et al. In-situ ultrafast construction of zinc tungstate interface layer for highly reversible zinc anodes. *Angew. Chem. Int. Ed.* **2024**, *63*, e202319661.
174. Gao, G.; Huo, X.; Li, B.; et al. Customizing water-scarce, zinc ion-rich Helmholtz plane of zinc anode for Ah-scale Zn metal batteries. *Energy Environ. Sci.* **2024**, *17*, 7850.
175. Huang, W.; Huang, Y.; Huang, X.; et al. 3D leaf-like copper-zinc alloy enables dendrite-free zinc anode for ultra-long life aqueous zinc batteries. *Small* **2024**, *20*, 2404294.
176. Ling, W.; Nie, C.; Wu, X.; et al. Ion sieve interface assisted zinc anode with high zinc utilization and ultralong cycle life for 61 Wh/kg mild aqueous pouch battery. *ACS Nano* **2024**, *18*, 5003.
177. Peng, Z.; Yan, H.; Zhang, Q.; et al. Stabilizing zinc anode through ion selection sieving for aqueous Zn-ion batteries. *Nano Lett.* **2024**, *24*, 9137.
178. Shu, C.; An, Y.; Liu, Y.; et al. Construction of corrosion-resistant and dendrite-free zinc anode by coating nano-ceriumoxide for highly stable zinc battery. *Chem. Eng. J.* **2025**, *509*, 161096.
179. Zhao, M.; Lv, Y.; Qi, J.; et al. Crystallographic reorientation induced by gradient solid-electrolyte interphase for highly stable zinc anode. *Adv. Mater.* **2024**, *36*, 2412667.
180. Cao, Z.; Zhang, H.; Song, B.; et al. Angstrom-level ionic sieve 2D-MOF membrane for high power aqueous zinc anode. *Adv. Funct. Mater.* **2023**, *33*, 2300339.
181. Hu, Z.; Zhou, L.; Meng, D.; et al. Surface engineering for ultrathin metal anodes enabling high performance Zn-ion batteries. *ACS Appl. Mater. Interfaces* **2023**, *15*, 5161.
182. Lee, J.; Kim, R.; Kim, S.; et al. Dendrite-free Zn electrodeposition triggered by interatomic orbital hybridization of Zn and single vacancy carbon defects for aqueous Zn-based flow batteries. *Energy Environ. Sci.* **2020**, *13*, 2839.
183. Luo, Y.; Hu, J.; Cai, S.; et al. Chelate-capped nano-$AgZn_3$ dual interphase remodeling the local environment for reversible dendrite-free zinc anode. *Small* **2023**, *19*, 2303268.
184. Pan, Z.; Cao, Q.; Gong, W.; et al. Zincophilic 3D ZnOHF nanowire arrays with ordered and continuous Zn^{2+} ion modulation layer enable long-term stable Zn metal anodes. *Energy Storage Mater.* **2022**, *50*, 435.
185. Qin, H.; Kuang, W.; Huang, D.; et al. Achieving high-rate and high-capacity Zn metal anodes via a three-in-one carbon protective layer. *J. Mater. Chem. A* **2022**, *10*, 17440.
186. Liu, P.; Zhang, Z.; Hao, R.; et al. Ultra-highly stable zinc metal anode via 3D-printed g-C_3N_4 modulating interface for long life energy storage systems. *Chem. Eng. J.* **2021**, *403*, 126425.
187. Song, Q.; Liang, J.; Liu, S.; et al. Negatively charged insulated boron nitride nanofibers directing subsurface zinc deposition for dendrite-free zinc anodes. *Nano Res.* **2023**, *16*, 403.
188. Chen, Z.; Shen, T.; Xiao, X.; et al. An ultrahigh-modulus hydrogel electrolyte for dendrite-free zinc ion batteries. *Adv. Mater.* **2024**, *36*, 2413268.
189. Guo, S.; Yan, M.; Xu, D.; et al. Anti-freezing hydrogel electrolyte with regulated hydrogen bond network enables high-rate and long cycling zinc batteries. *Energy Environ. Sci.* **2025**, *18*, 418.
190. Li, J.; Zhang, H.; Liu, Z.; et al. Boosting dendrite-free zinc anode with strongly polar functional group terminated hydrogel electrolyte for high-safe aqueous zinc-ion batteries. *Adv. Funct. Mater.* **2024**, *35*, 2412865.

191. Luo, F.; Yang, S.; Wu, Q.; et al. Hydrogel electrolytes with an electron/ion dual regulation mechanism for highly reversible flexible zinc batteries. *Energy Environ. Sci.* **2024**, *17*, 8570.
192. Shen, Z.; Liu, Y.; Li, Z.; et al. Highly-entangled hydrogel electrolyte for fast charging/discharging properties in aqueous zinc ion batteries. *Adv. Funct. Mater.* **2024**, *35*, 2406620.
193. Shen, Z.; Zhai, Z.; Liu, Y.; et al. Hydrogel electrolytes based rechargeable zinc ion batteries under harsh conditions. *Nano-Micro Lett.* **2025**, *17*, 227.
194. Wang, Y.; Liang, B.; Li, D.; et al. Hydrogel electrolyte design for long-lifespan aqueous zinc batteries to realize a 99% Coulombic efficiency at 90 °C. *Joule* **2025**, *9*, 101944.
195. Xiang, Z.; Li, Y.; Cheng, X.; et al. Lean-water hydrogel electrolyte with improved ion conductivity for dendrite-free zinc-Ion batteries. *Chem. Eng. J.* **2024**, *490*, 151524.
196. Xia, H.; Zhang, W.; Miao, C.; et al. Ultra-thin amphiphilic hydrogel electrolyte for flexible zinc-ion paper batteries. *Energy Environ. Sci.* **2024**, *17*, 6507.
197. Xiong, Y.; Cheng, H.; Jiang, Y.; et al. A novel water-reducer-based hydrogel electrolyte for robust and flexible Zn-I2 battery. *Energy Storage Mater.* **2025**, *74*, 103981.
198. Xu, X.; Li, S.; Yang, S.; et al. Superelastic hydrogel electrolyte incorporating helical protein molecules as zinc ion transport pathways to enhance cycling stability of zinc metal batteries. *Energy Environ. Sci.* **2024**, *17*, 7919.
199. Abbasi, A.; Xu, Y.; Abouzari-Lotf, E.; et al. Phosphonated graphene oxide-modified polyacrylamide hydrogel electrolytes for solid-state zinc-ion batteries. *Electrochim. Acta* **2022**, *435*, 141365.
200. Chen, Y.; Zhang, Z.; Cai, P.; et al. Polyoxotungstate featuring zinc-ion-triggered structural transformation as an efficient electrolyte additive for aqueous zinc-ion batteries. *Angew. Chem. Int. Ed.* **2024**, *137*, e202420284.
201. Dong, J.; Zhou, G.; Ding, W.; et al. Machine learning-assisted benign transformation of three zinc states in zinc ion batteries. *Energy Environ. Sci.* **2025**, *18*, 4872.
202. Feng, W.; Zhang, L.; Cheng, Y.; et al. Screening and design of aqueous zinc battery electrolytes based on the multimodal optimization of molecular simulation. *J. Phys. Chem. Lett.* **2025**, *16*, 3326.
203. Huang, S.; Fu, H.; Kwon, H.M.; et al. Stereoisomerism of multi-functional electrolyte additives for initially anodeless aqueous zinc metal batteries. *Nat. Commun.* **2025**, *16*, 6117.
204. Luo, H.; Gou, Q.; Zheng, Y.; et al. Machine learning-assisted high-donor number electrolyte additive screening toward construction of dendrite-free aqueous zinc-ion batteries. *ACS Nano* **2025**, *19*, 2427.
205. Shang, Y.; Kundi, V.; Pal, I.; et al. Highly potent and low-volume concentration additives for durable aqueous zinc batteries: Machine learning-enabled performance rationalization. *Adv. Mater.* **2024**, *36*, 2309212.
206. Wu, Q.; Huang, J.; Zhang, J.; et al. Multifunctional cellulose nanocrystals electrolyte additive enable ultrahigh-rate and dendrite-free Zn anodes for rechargeable aqueous zinc batteries. *Angew. Chem. Int. Ed.* **2024**, *63*, e202319051.
207. Xie, Z.; Chen, N.; Zhang, M.; et al. Carbonate-assisted chaotropic electrolyte for zinc ion battery with wide temperature operation. *ACS Energy Lett.* **2024**, *9*, 3380.
208. Chen, Y.; Gong, F.; Deng, W.; et al. Dual-function electrolyte additive enabling simultaneous electrode interface and coordination environment regulation for zinc-ion batteries. *Energy Storage Mater.* **2023**, *58*, 20.